ADVANCED MATERIALS
www.advmat.de

Many-Body Complexes in 2D Semiconductors

Jiajie Pei, Jiong Yang, Tanju Yildirim, Han Zhang, and Yuerui Lu**

2D semiconductors such as transition metal dichalcogenides (TMDs) and black phosphorus (BP) are currently attracting great attention due to their intrinsic bandgaps and strong excitonic emissions, making them potential candidates for novel optoelectronic applications. Optoelectronic devices fabricated from 2D semiconductors exhibit many-body complexes (exciton, trion, biexciton, etc.) which determine the materials optical and electrical properties. Characterization and manipulation of these complexes have become a reality due to their enhanced binding energies as a direct result from reduced dielectric screening and enhanced Coulomb interactions in the 2D regime. Furthermore, the atomic thickness and extremely large surface-to-volume ratio of 2D semiconductors allow the possibility of modulating their inherent optical, electrical, and optoelectronic properties using a variety of different environmental stimuli. To fully realize the potential functionalities of these many-body complexes in optoelectronics, a comprehensive understanding of their formation mechanism is essential. A topical and concise summary of the recent frontier research progress related to many-body complexes in 2D semiconductors is provided here. Moreover, detailed discussions covering the aspects of fundamental theory, experimental investigations, modulation of properties, and optoelectronic applications are given. Lastly, personal insights into the current challenges and future outlook of many-body complexes in 2D semiconducting materials are presented.

1. Introduction

The discovery of graphene[1] opened up a door to the world of 2D materials. Afterward, a great number of 2D materials with intriguing properties have been reported, covering metals, semiconductors, and insulators.[2] Among 2D semiconducting materials, transition metal dichalcogenides (TMDs)[3,4] and black phosphorus (BP)[5,6] have drawn tremendous attention in the "postgraphene age" due to their intrinsic bandgaps and unique properties that possess huge potential in optoelectronic applications. The optoelectronic properties of 2D semiconductors change remarkably when they are scaled down to single or a few atomic layers, for example, the indirect-to-direct bandgap transition in TMDs[7,8] and the layer-dependent direct bandgap energies in BP.[9,10] Another consequence of the reduced dimensionality is the increased binding energy of the many-body complexes inside a 2D semiconductor caused by dramatically reduced dielectric screening and significantly enhanced Coulomb interactions, and this enables their stable existence at room temperature.[11,12] Moreover, theoretical calculations and experimental measurements revealed that their binding energies could reach a scale of several hundred millielectronvolts for excitons and tens of millielectronvolts for trions and biexcitons.[13–18] The surprisingly large binding energy is a result of electrons and holes tightly bound in many-body excitonic states instead of appearing as electron–hole plasma. Thus, the optical and electrical properties of 2D semiconductors are closely related to these excitonic structures.[19,20] To fully realize the potential functionalities of 2D semiconductors in optoelectronics, a comprehensive understanding of their intrinsic many-body complexes is necessary.

Recently, there has been large progress toward the theoretical and experimental study of many-body complexes.[21–30] However, a general agreement still remains elusive about the exact formation mechanism and binding energies of these excitonic structures.[13–16] This needs to be resolved as it is substantial to give a summary on recent progress to draw conclusions. Currently, a review article that summarizes the research process of many-body complexes in 2D semiconductors is absent. Existing reviews mainly focused on the overall progress,[31,32] synthesis methods,[33,34] optoelectronic applications,[3,4] or other specific aspects for a particular type of 2D material.[5,6,35–37] Additionally, in spite of the semiconducting nature of both TMDs and

Dr. J. Pei, Prof. H. Zhang
Collaborative Innovation Center for Optoelectronic Science and Technology
Key Laboratory of Optoelectronic Devices and Systems of Ministry of Education and Guangdong Province
College of Optoelectronic Engineering
Shenzhen University
Shenzhen 518060, P. R. China
E-mail: hzhang@szu.edu.cn
Dr. J. Yang, Dr. T. Yildirim
College of Chemistry and Environmental Engineering
Shenzhen University
Shenzhen 518060, P. R. China
Dr. J. Yang, Dr. T. Yildirim
Key Laboratory of Optoelectronic Devices and Systems of Ministry of Education and Guangdong Province
College of Optoelectronic Engineering
Shenzhen University
Shenzhen 518060, P. R. China
Prof. Y. Lu
Research School of Engineering
The Australian National University
Canberra ACT 2601, Australia
E-mail: yuerui.lu@anu.edu.au

DOI: 10.1002/adma.201706945

BP, they can exhibit significantly different optical properties such as the thickness-dependent indirect/direct bandgap structures,[8,10,38] in-plane isotropic/anisotropic properties,[22,23] and a quasi-1D/2D excitonic nature.[15,39] A comparative study of these behaviors would further contribute to an in-depth understanding of the fundamental physics in 2D semiconductors.

This review provides a topical and concise summary toward recent frontier research progress related to the many-body complexes in 2D semiconductors. The many-body complexes are discussed in detail covering the aspects of fundamental theory, experimental studies, modulation of intrinsic properties, and optoelectronic applications. First, the electronic structures and excitonic effects for TMDs and BP are summarized in the theoretical part. Then, a review of the major experimental techniques to characterize the many-body complexes and their binding energies as well as their diffusion dynamics are discussed. This is followed by a detailed review of three categories for modulating the properties of 2D semiconducting materials, namely, bandgap engineering, defect engineering, and environmental engineering. Afterward, several representative optoelectronic applications are introduced according to their working principles based on recombination/separation of the electrons and holes from excitonic complexes. Lastly, personal insights into the challenges and outlooks in this field are given. The aim of this review is to provide researchers with an idea on how to modify the optical properties and extend the functionality of 2D semiconductors. The authors also aim to provide further suggestions toward future research directions that may attract broad interest from the fields of chemistry, physics, material science, and engineering.

Jiajie Pei is currently a postdoctoral researcher of Collaborative Innovation Center for Optoelectronic Science and Technology at Shenzhen University. He received his bachelor's degree in mechanical engineering from Beijing Institute of Technology in 2010. Then, he continued to achieve his Ph.D. degree under the cotraining between Beijing Institute of Technology and Australia National University. His research interests include the synthesis and characterization, optical properties, and optoelectronic devices of 2D materials.

Han Zhang is currently a distinguished professor and the director of Shenzhen Engineering Laboratory of Phosphorene and Optoelectronics, Shenzhen University. He received his B.S. degree from Wuhan University in 2006 and Ph.D. from Nanyang Technological University in 2010. His current research focuses on the ultrafast-, nonlinear-, and biophotonics of 2D materials.

Yuerui Lu received his Ph.D. degree from Cornell University, the school of Electrical and Computer Engineering, in 2012. He holds a B.S. degree from department of Applied Physics at University of Science and Technology of China. His research interests include MEMS/NEMS sensors and actuators, nanomanufacturing technologies, renewable energy harvesting, biomedical novel devices, nanomaterials, nanoelectronics, etc.

2. Fundamental Theory

2.1. Electronic Structures

2D semiconductors such as TMDs and BP are currently attracting great attention due to their moderate bandgaps ranging from 0.3 to 2.5 eV, this makes them promising candidates for novel optoelectronic applications in the visible to near-infrared regime.[6,37] Electronic band structures are the theoretical basis for the investigation of many-body effects in 2D semiconductors. The band structures of TMDs and BP are obtained by using density functional theory (DFT) calculations based on their atomic structures.[8,10,39–42]

2.1.1. Transition Metal Dichalcogenides

TMDs consist of an inner layer of transition metal atoms (M) sandwiched between two layers of chalcogen atoms (X) in a trigonal prismatic structure with a formula MX_2 (where M = Mo, W, etc., and X = S, Se, etc.). The crystal structure of TMDs is schematically shown in **Figure 1**a. The lattice parameters *a*, *u*, and *c*′ are used for the calculation of band structures where *a* is the in-plane distance between the nearest neighboring X atoms, *u* is the distance between the M and X planes within a layer, and *c*′ is the distance between the M planes of two adjacent TMD layers. The value of *a*, *u*, and *c*′ parameters for four widely investigated TMDs (MoS_2, WS_2, $MoSe_2$, and WSe_2) are given in **Table 1**. The calculated band structures of monolayer and bilayer MX_2 are shown in Figure 1b. It can be seen that all the monolayers have direct bandgaps at the K–K point of the Brillouin zone, whereas the bilayer becomes an indirect bandgap structure with lower-energy transitions at the Γ–Q points.[8] The direct/indirect energy gaps for monolayer and bilayer TMDs are summarized in Table 1. Noticeably, a splitting

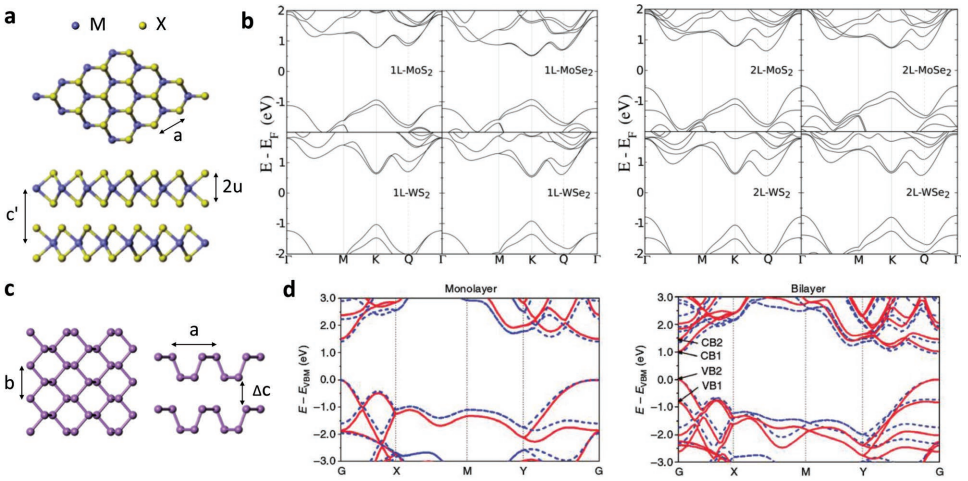

Figure 1. Electronic structures of TMDs and BP. a) Top view (top) and side view (bottom) of TMDs with MX_2 lattice structure (where M = Mo, W and X = S, Se). b) Band structures of monolayer (left) and bilayer (right) TMDs. c) Top view (left) and side view (right) of BP lattice structure. d) Band structures of monolayer (left) and bilayer (right) BP. b) Reproduced with permission.[8] Copyright 2014, Wiley-VCH. d) Reproduced with permission.[10] Copyright 2013, Nature Publishing Group.

of the conduction band (see the Q point) and the valence band (see the K point) is observed for all cases due to the spin–orbit coupling (SOC) effect. The splitting energy at the valence band of WS_2/WSe_2 compounds is ≈400 meV, which is much larger than that of $MoS_2/MoSe_2$ compounds (≈150 meV), resulting from the different compounds W and Mo.[8] The splitting of the conduction band at Q points enlarges from monolayer to bilayer, whereas it remains almost unchanged at the K point of the valence band.

2.1.2. Black Phosphorus

BP has a puckered orthorhombic lattice structure with P atoms distributed on two planes and each P atom connected to three neighboring atoms as shown in Figure 1c.[10] The lattice parameters *a*, *b*, and Δ*c* are used for band structure calculation, where *a* and *b* are the lattice constant along the armchair and zigzag directions, respectively, and Δ*c* is the interlayer spacing between two adjacent BP layers. The calculated electronic band structures of monolayer and bilayer BP are shown in Figure 1d. Note that the lattice parameters of BP given in Table 1 are for bulk materials. In contrast to the invariable value of TMDs from bulk to monolayers, parameter *a* for BP increases while parameter *b* gradually decreases when the thickness is reduced. The abrupt reduction of the lattice parameter *a* from monolayer to bilayer is due to wavefunction overlapping instead of van der Waals forces that play the major role in interlayer interactions.[10] This interlayer interaction results in two additional bands (VB2 and CB2) emerging around the gap at the G point and a remarkable reduction of bandgap energy from monolayer to bilayer but the bandgap structure still remains direct, different from the direct-to-indirect bandgap transition in TMDs from monolayer to bilayer. Moreover, no band splitting is observed at the G point of the Brillouin zone because of the small effective nuclear charge (Z_{eff}) of the P atom and the weak variation of the charge gradient in BP.[10] The bandgap energy of BP decreases continuously as the layer number increases because of the larger dispersion of the conduction band and the valence band caused by stronger interactions in thicker layers. The bandgap is estimated to vary from around 1.51 eV in monolayer BP (also termed as phosphorene) to around 0.3 eV in bulk form via the HSE06 method.[10] However, using the G_0W_0 method, the bandgap could reach 2.0 eV in phosphorene and 0.3 eV in bulk BP, covering the visible to near-infrared spectral regime.[6] Compared with the experimental data,[29] it has been found that the G_0W_0 method provides more accurate predictions for the bandgap structure in BP.

Table 1. Lattice parameters and bandgap energies of TMDs and BP.

	a [Å]	$u/b^{a)}$ [Å]	$c'/\Delta c^{a)}$ [Å]	Bandgap [eV]		
				Monolayer	Bilayer	Bulk
MoS_2	3.160	1.586	6.140	1.715	1.710, 1.198	1.679, 0.788
WS_2	3.153	1.571	6.160	1.659	1.658, 1.338	1.636, 0.917
$MoSe_2$	3.288	1.664	6.451	1.413	1.424, 1.194	1.393, 0.852
WSe_2	3.260	1.657	6.422	1.444	1.442, 1.299	1.407, 0.910
BP	4.470	3.340	3.200	1.510	1.020	0.360

[a)]Parameters *u* and *c'* are used for TMDs,[8] and *b* and Δ*c* are used for BP.[10]

2.2. Excitonic Effects

Due to reduced dielectric screening in the 2D limit, excitonic effects become extremely strong in 2D semiconductors. Optically excited electrons and holes between valence and conduction bands are bound together by Coulomb interactions forming excitons (one electron and one hole), trions

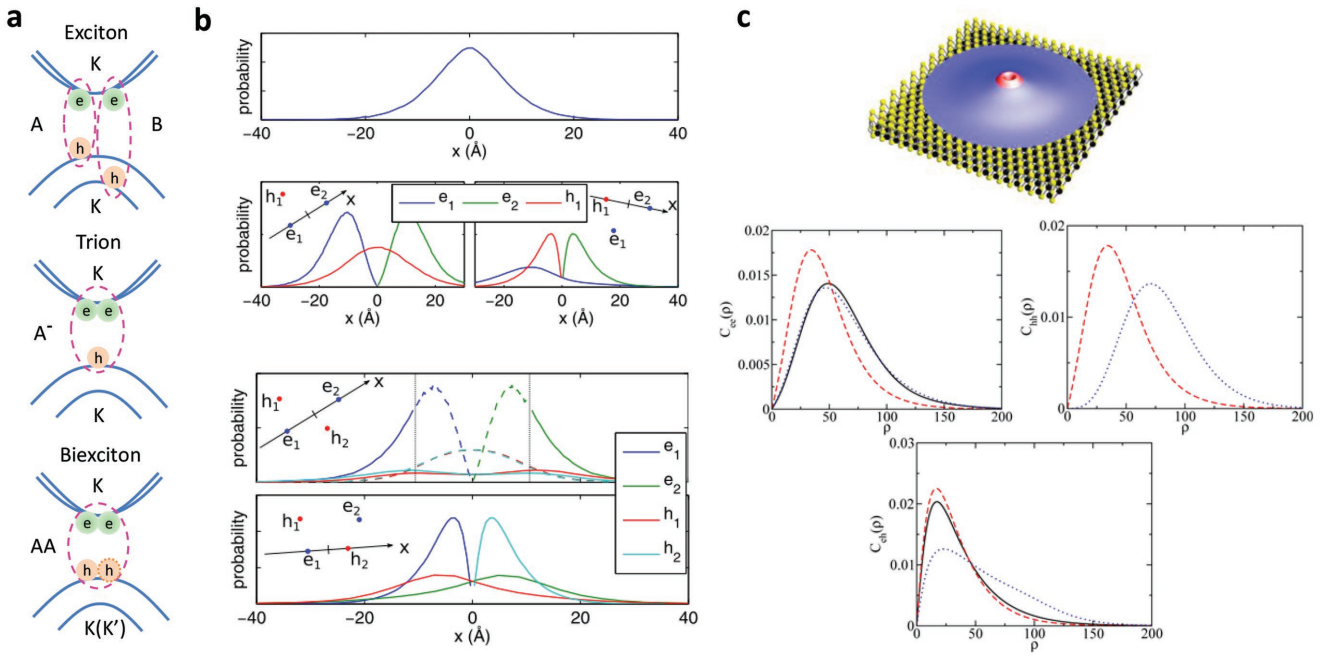

Figure 2. Theoretical calculation of many-body complexes. a) Illustration of the exciton (top), trion (middle), and ground-state biexciton (bottom) systems constructed from the electrons in the conduction band and holes in the valence band. In biexciton system, the solid and dashed circles h represent that the two holes could be from different valleys K and K′ when they have opposite spins. b) Particle coordinate distributions in the case of the exciton (top), trion (middle), and ground-state biexciton (bottom). c) Illustration of the excited-state biexciton system (top) and electron–electron (middle left), hole–hole (middle right), and electron–hole (bottom) correlation functions for the WSe_2 trion (black solid line), ground-state biexciton (red dashed line), and L = 0 excited-state biexciton (blue dotted line). b) Reproduced with permission.[15] Copyright 2015, American Physical Society. c) Reproduced with permission.[16] Copyright 2015, American Chemical Society.

(two electrons and one hole, or two holes and one electron), and biexcitons (two electrons and two holes). The existence of excitons and higher-order excitonic quasiparticles in 2D semiconductors has attracted great interest from several theoretical studies.[21–23,43–47] Excitons in TMDs are called valley excitons because they occur at the K and K′ points of the Brillouin zones, this is different from the transition at the Γ point in conventional semiconductors such as GaAs.[8] The splitting of the valence band at the K point results in two excitonic features (A and B excitons) in the photoluminescence (PL) spectrum and a schematic plot of A and B excitons are shown in **Figure 2**a. When additional charges (electron or hole) are attached to a neutral exciton, a few-particle (trion, biexciton, etc.) system is formed. The binding strength can be estimated using an effective mass model,[15,21] stochastic variational method (SVM),[16] or the Bethe–Salpeter equation (BSE).[39,40,43] Within the effective mass approach, the path integral Monte Carlo (PIMC) method exhibits good performance for an accurate determination of exciton and trion complexes in TMDs.[15] By using this method, relevant parameters are calculated using DFT and the binding energies and mean particle distances are determined. Figure 2b shows the *x*-coordinate distribution of all particles when the *x* axis is chosen to be along the connection of two particles with the origin at their center of mass. For excitons, the electron distribution is similar to that of the hydrogen 1s state when the hole is fixed at the origin. For negative trions, the hole is largely located between the electrons. For biexcitons, there is one hole located close to each electron when the distance between electrons is large; however, when the distance between electrons is small, the extent of the hole wave function becomes too large to make such a distinction.[15] The calculated binding energies for these complexes in TMDs are given in **Table 2**. It should be noted that they were calculated in a vacuum whereas these values would decrease as the dielectric screening increases.[15] The binding energies of the complexes are remarkably large indicating extremely strong Coulomb interactions in these TMD semiconductors.

Despite the correctly estimated binding energies of excitons and trions by the effective mass model, the predicted binding energies of biexcitons are unexpectedly smaller than that of trions, which contradicts experimental observations.[13,14] Varga and co-workers ascribed this binding energy discrepancy due to the biexciton ground state.[16] Using the high-accuracy stochastic variational method, they found that a biexciton has bound excited states and the binding energy of the L = 0 excited state is in good agreement with experimental values. This excited state corresponds to a hole attached to a negative trion from a faraway distance (as illustrated in Figure 2c) since the electron–electron correlation functions of the trion and excited-state biexciton are almost identical (Figure 2d).[16] The hole–hole correlation functions are different for the ground and excited states. The electron–hole correlation functions are very similar for trions and the ground state, while the peak of the excited states is half the amplitude but at the same position, this indicates that one of the holes exists in a trion-like structure. The tail of the excited-state correlation function extends far beyond the other correlation functions, showing that another hole exists somewhere outside of the trion.[16] Consequently, the

Table 2. Excitonic binding energies of the complexes (meV).

	MoS_2		$MoSe_2$		WS_2		WSe_2		BP
	Theory								
Ref.	[15]	[16]	[15]	[16]	[15]	[16]	[15]	[16]	[22]
Exciton A	526.5	555	476.9	480	509.8	523	456.4	470	743.9
Trion A^-	32.0	34	27.7	28	33.1	34	28.5	30	51.6
Trion A^+	31.6	–	27.8	–	33.5	–	28.5	–	51.6
Biexciton AA	22.7	22	19.3	18	23.9	24	20.7	20	40.9
Biexciton AA*	–	69	–	58	–	67	–	59	–
	Experiment								
Exciton A	500,[51] 570[60]		550,[61] 590[65]		320,[18] 700[25]		370,[30] 720[65]		300[29]
Trion A^-/A^+	18,[12] 30[26]		30[11,67]		30[52]		30,[64] 28[65]		100[29]
Biexciton AA/AA*	70,[51] 60[26]		60[57]		65,[52] 45[13]		52[14]		–

excited-state biexciton is energetically favorable and more stable than the ground-state biexciton. The present SVM method can reproduce the binding energies of excitons, trions, and ground-state biexcitons with great accuracy compared to previous calculation results (as shown in Table 2).

BP has also been investigated by first-principles GW-BSE simulations.[39] The quasiparticle bandgap and optical spectra for few-layer and bulk BP have been investigated. Significant many-electron effects and highly anisotropic optical responses have been observed in BP, resulting from their unique quasi-1D band dispersions. Few-layer BP strongly absorbs light polarized along its lattices armchair direction, but they are almost transparent to light polarized along the zigzag direction. Enhanced many-electron effects are essential in shaping their bandgaps and optical responses because of the anisotropic band dispersions and their effectively quasi-1D nature.[39] Trions and biexcitons in BP have also been investigated using the effective mass theory. Trions are predicted to have remarkably high binding energies (nearly twice as that of TMDs, see Table 2) and an elongated electron–hole structure with a preference of alignment along the armchair direction, where the effective masses are smaller.[22] The anisotropic effective masses of electrons and holes would result in anisotropic transport properties of excitons and trions in BP.

3. Experimental Study

3.1. Characterization of Complexes

When a 2D semiconductor is illuminated by light with photon energy larger than its bandgap, electrons will be excited from the valence band to the conduction band, followed by relaxation and recombination of electron and hole pairs, resulting in new photon emissions with energy equal to the optical bandgap of this material (see Figure 2a); this behavior can be used to efficiently detect the electronic bandgaps of 2D semiconductors. It should be noted that there could be an energy difference between the optical and electronic bandgaps giving rise to the Stokes shift, especially for 2D semiconductors where excitons are tightly bound and this is discussed in detail in the following part. For monolayer TMDs at room temperature, two feature peaks are detected in the optical absorption (reflectance) spectra, corresponding to A and B direct excitonic transitions associated with the SOC-induced splitting of the valence band edge,[48] where A excitonic transitions are more significant in the PL process as shown in **Figure 3**a. For few-layer TMDs, an additional PL peak at the lower-energy side (several hundred millielectronvolts) can be observed due to indirect transitions. BP exhibits a broad PL spectra from 700 nm (monolayer) to 1550 nm (five-layer) depending on the thickness as shown in Figure 3b. The wavelength could be extended to 4 μm in the bulk form, corresponding to a 0.3 eV photon energy. Under cryogenic temperatures, the PL spectra becomes broad with multiple peaks due to simultaneously emerging multiple excitonic states, such as excitons, trions, biexcitons, and localized states (Figure 3c). It is critical to distinguish them experimentally in order to gain insights into these complexes and explore their functionalities.[11–14,26–30,49–55] The commonly used methods are power-dependent PL analysis (Figure 3c), time-resolved PL (TRPL) trace (lifetime) analysis (Figure 3d), and circularly polarized emission component analysis (Figure 3e).

For power-dependent PL analysis, PL intensities as a function of several excitation powers are recorded. First, multipeak fitting is used to analyze the components of the spectra. It is observed that the PL growth rate for each component varies with the increase of excitation power. Then, the integrated intensities of all components as functions of the excitation power are plotted in logarithmic coordinates as shown in Figure 3c. By fitting the data with a power law, it is found that the emissions from exciton and trion states increase linearly (slope $\alpha \approx 1$) with the excitation power. However, the emission from localized states (defect) normally presents sublinear behavior (slope $\alpha < 0.8$) because the defect-induced emission will saturate at high excitation powers.[56] In contrast, the integrated intensity of biexciton emission grows superlinearly (slope $\alpha > 1.2$, as various slopes varying from 1.2 to 1.9 have been experimentally observed[13,14,57]) as a function of the excitation power.[13] Moreover, it is found that exciton and trion PL peaks have the narrowest full width at half-maximum (FWHM), and the FWHM

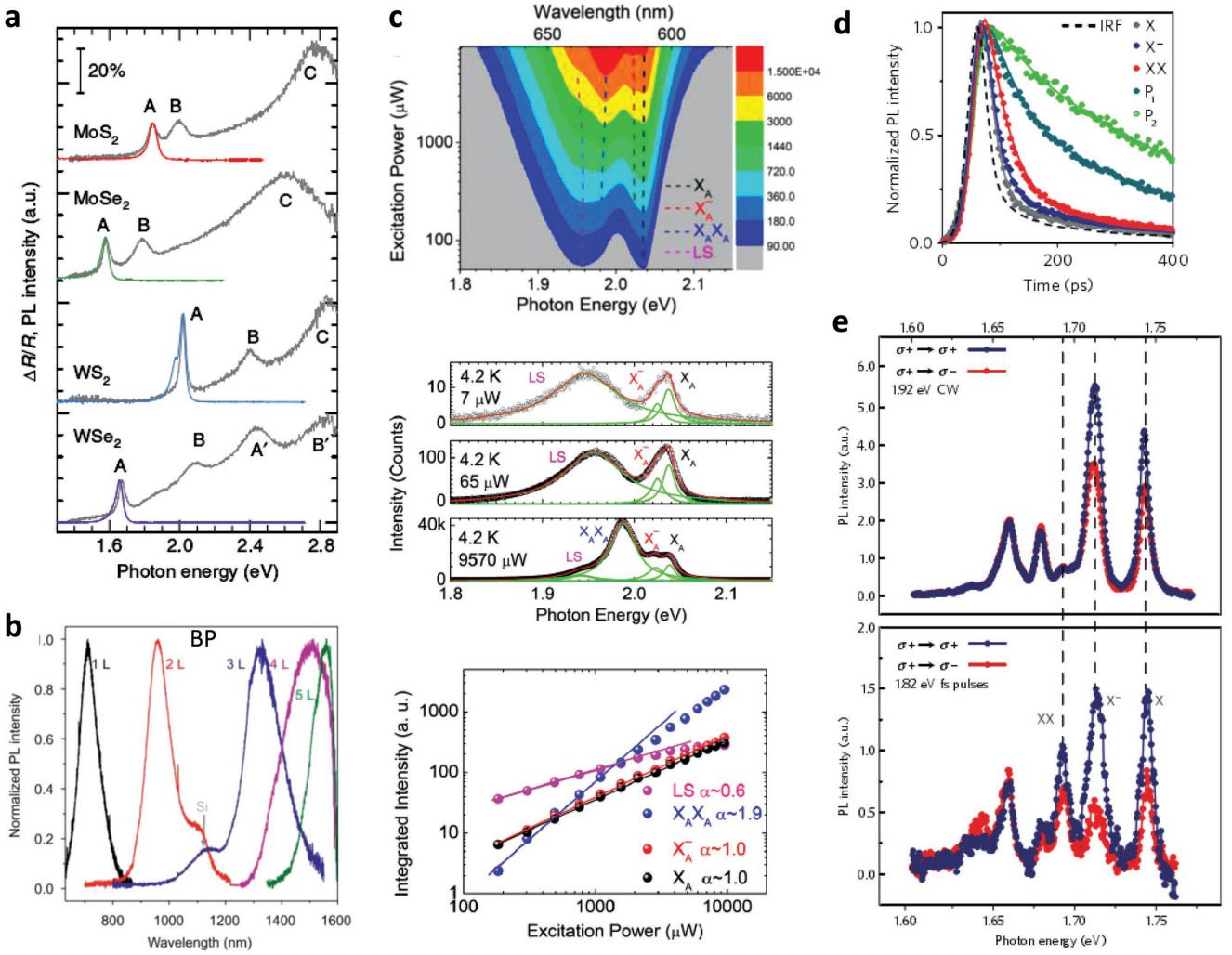

Figure 3. Experimental characterization of the many-body complexes. a) PL spectra (red, green, blue, and purple curves) and differential reflectance spectra (gray curves) of monolayer TMDs. b) PL spectra of monolayer to five-layer BP. c) Power-dependent analysis for many-body complexes. Top: PL mapping versus excitation power and photon energy for a monolayer WS_2 at 4.2 K. Middle: PL spectra at various excitation powers and their multi-peak fitting results. Bottom: Log–log plots of integrated intensities of four emission components versus excitation power. d) Time-resolved PL traces (lifetime) analysis for many-body complexes. e) Circularly polarized emission components analysis for many-body complexes. Top: PL spectra for low exciton density with CW excitation at a photon energy of 1.92 eV. Bottom: PL spectra for high exciton density with pulsed excitation at a photon energy of 1.82 eV. a) Reproduced with permission.[28] Copyright 2014, Nature Publishing Group. b) Reproduced with permission.[29] Copyright 2015, Nature Publishing Group. c) Reproduced with permission.[13] Copyright 2015, American Chemical Society. d,e) Reproduced with permission.[14] Copyright 2015, Nature Publishing Group.

of biexciton peaks is about twice that of an exciton. The localized states have a much broader PL peak compared to excitons, trions, and biexcitons.

Carrier lifetime is a very critical parameter for 2D semiconductors. TRPL traces can be used to characterize the carrier lifetime of each excitonic state. All of the time traces can be fitted to a rapid rise, comparable to the instrumental response but the decay rates strongly differ.[14] The lifetime of exciton, trion, and biexciton states is in the same order of magnitude, whereas the lifetime of defect states could be an order of magnitude larger (Figure 3d). This result provides further evidence to distinguish defect states from other excitonic states. The nature of excitonic states and the valley occupancy of these states can be probed via the polarization characteristics from the PL spectra.[14] Taking monolayer WSe_2 as an example (Figure 3e), the exciton (shown as X) and trion (shown as X^-) peaks exhibit significant circular polarization under both continuous-wave (CW) laser and pulsed excitations. However, the defect-related emission peaks (located at ≈1.66 and ≈1.68 eV in Figure 3e) show no measurable circular polarization characteristics. Particularly, the circularly polarized biexciton emission (shown as XX) can be observed at a high excitation density (under pulsed laser) but diminishes at lower excitation densities (under CW laser). Moreover, biexciton emissions with both the same and opposite circularly polarized states can be observed for near-resonant excitation, which suggests that both intra- and intervalley biexcitons can be formed in monolayer WSe_2 although the biexcitons formed from the former are expected to arise more strongly than the latter.[14] These results provide additional evidence for the identification of excitonic states by circularly polarized PL measurements. In

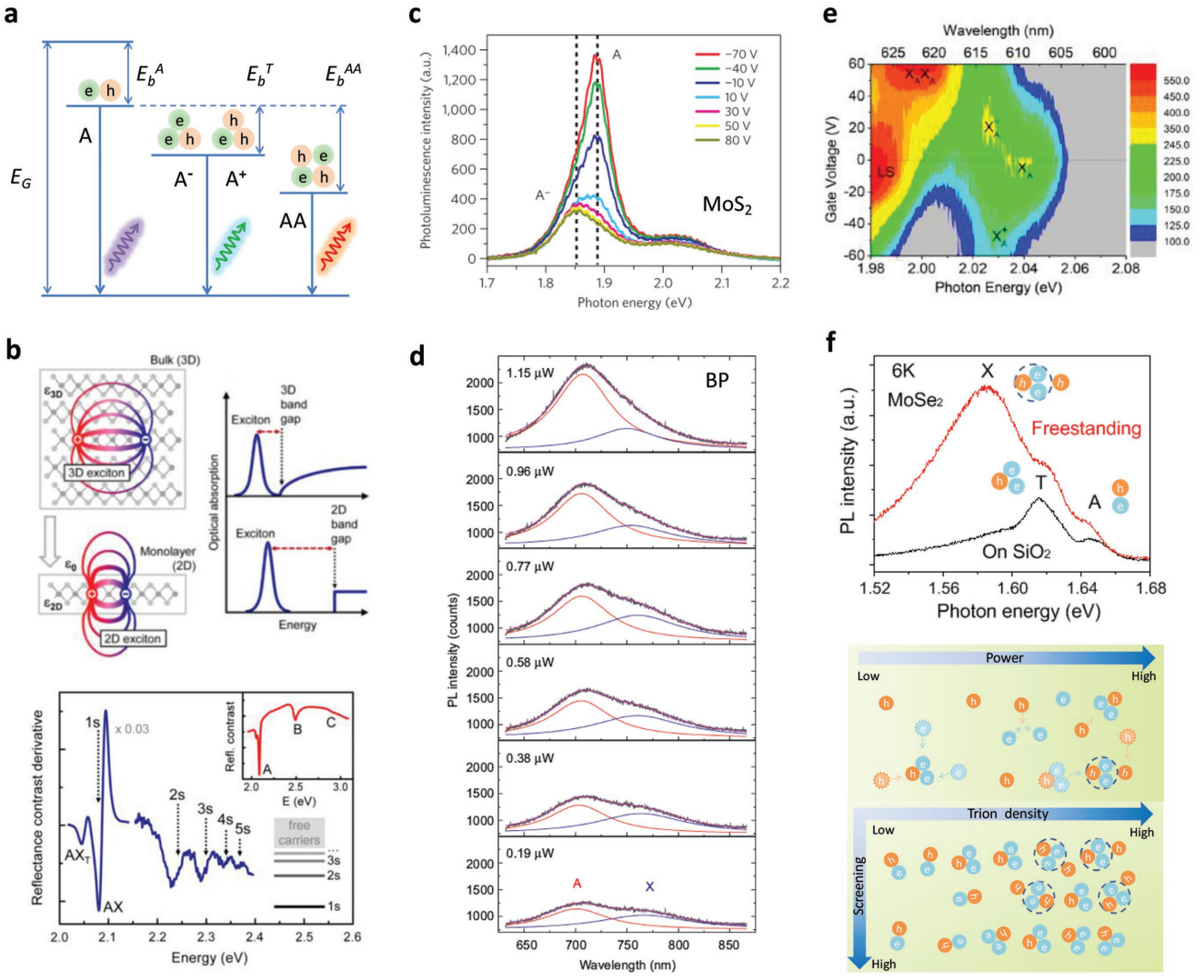

Figure 4. Binding energies of the many-body complexes. a) Illustration of the binding energies of exciton, trion, and biexciton. b) Measurement of the exciton binding energy. Top: Illustration of the increase of the exciton binding energy and the bandgap from 3D bulk to 2D monolayer. Bottom: The derivative of the reflectance contrast spectrum $(d/dE)(\Delta R/R)$ of the WS_2 monolayer, showing the excitonic Rydberg series. c) Measurement of the trion binding energy for MoS_2 by electrical doping. d) Measurement of the trion binding energy for BP by optical doping. e) Measurement of the trion and biexciton binding energies for WS_2 by electrical and optical doping. f) Formation mechanism study of excited-state biexciton. Top: Measured PL spectra from free-standing and SiO_2-supported bilayer $MoSe_2$ at 6 K. Bottom: Schematic plots showing the relationship between the density of excited-state biexciton with dielectric screening, density of trions, and excitation power. b) Reproduced with permission.[18] Copyright 2014, American Physical Society. c) Reproduced with permission.[12] Copyright 2012, Nature Publishing Group. d) Reproduced with permission.[29] Copyright 2015, Nature Publishing Group. e) Reproduced with permission.[13] Copyright 2015, American Chemical Society. f) Reproduced with permission.[57] Copyright 2017, American Chemical Society.

addition, the valley polarization properties of these excitonic features also offer the opportunity to study and manipulate the spin dynamics in layered TMDs. For more details about the spin and pseudospins in TMDs, readers are referred to other specialized reviews.[58]

3.2. Binding Energies

When disassembling compounds from a many-body system into free carriers a certain amount of energy is required, namely, the binding energy, which reflects the degree of binding of the compounds. The exciton binding energy (E_b^A) is the energy difference between the electronic bandgap (E_g) and optical bandgap (E_{opt}) and is schematically illustrated in **Figure 4**a. More energy is needed for the formation of a trion as an additional electron/hole is bound to the exciton. This renders a difference in photon energy between the exciton and trion emissions, i.e., the trion binding energy (E_b^T). Similarly, the biexciton binding energy (E_b^{AA}) is the photon energy difference between the exciton and biexciton emissions (Figure 4a). Therefore, the binding energies for the exciton, trion, and biexciton can be expressed as $E_b^A = E_g - E_A$; $E_b^T = E_A - E_T$; $E_b^{AA} = E_A - E_{AA}$, respectively, where E_A, E_T, and E_{AA} are the emission energies of excitons, trions, and biexcitons.

The binding energy originating from the Coulomb interaction is almost negligible in the bulk form of 2D semiconductors. However, it is strongly increased when the thickness of material is thinned down to the 2D limit because of the quantum confinement effect.[59] The real-space origin of this behavior is schematically illustrated in Figure 4b. In contrast to bulk materials, the electron and hole form an exciton in monolayer TMDs that are strongly confined in the monolayer plane and additionally experience reduced screening due to a changed dielectric environment.[18,60,61] Therefore, the quasiparticle bandgap is expected to increase in the 2D limit and this allows for experimental measurement of exciton binding energy by the excitonic Rydberg series.[18,25] Photoluminescence excitation (PLE) measurement is commonly used to probe the excitonic Rydberg series (i.e., to detect the PL/reflectance spectra under different excitation photon energies).[62,63] On the high-energy side of the exciton 1s ground state, multiple additional peaks identified as the 2s, 3s, 4s, and 5s states of the A exciton can be observed in monolayer WS_2 as shown in Figure 4b.[18] The quasiparticle bandgap can be determined by fitting the excitonic peaks to a hydrogenic Rydberg series and the exciton binding energy can be calculated accordingly.[18] The experimentally measured exciton binding energies by Rydberg series as well as other methods for TMDs and BP are summarized in Table 2.

Through electrical/optical doping, switching between exciton, trion, and biexciton emissions have been observed in monolayer 2D semiconductors,[17,57,64–67] depending on the injected carrier types and carrier densities (Figure 4c–e). Trion and biexciton binding energies are therefore extracted based on the energy differences of PL emissions. A summary of their values and their corresponding references are given in Table 2. It has been measured that the trion binding energy of 2D TMDs is around 30 meV which is significantly larger than that in quasi-2D quantum wells (1–5 meV)[68] due to the reduced dimensionality. Similarly, the measured trion binding energy of phosphorene (≈100 meV)[29] is much larger than that of 2D TMDs but smaller than those measured in 1D carbon nanotubes (≈200 meV)[69] because the trions in phosphorene are theoretically predicted and experimentally confirmed to be confined in a quasi-1D space resulting from the anisotropic structure of phosphorene.[6] On the other hand, the measured biexciton binding energies in TMDs are around 60 meV,[13,14,52] which matches well with the theoretical prediction for excited-state biexcitons.[16] While two biexciton states are predicted by different theories, ground-state biexcitons have not yet been observed in experiments. One possible explanation is that the binding energies of the trions and ground-state biexcitons are rather close and they could not be easily distinguished in PL spectra. Furthermore, the excited state is a spatially extended state, which is more stable and energetically favorable than the ground state.[16] Biexciton emissions in phosphorene are still yet to reported in the literature.

The formation mechanism of excited-state biexcitons (Figure 4f) has been further investigated by experiments in freestanding atomically thin $MoSe_2$,[57] at room temperature the monolayer only exhibits excitonic emission features whereas the bilayer only exhibits trionic emissions. The weight of excited-state biexcitons in PL spectra was found to always increase with an increasing density of negative trions rather than excitons, which is exactly as predicted in theory.[16] Similar phenomena observed in other TMDs such as WS_2[13] (Figure 4e) and WSe_2[64] which provide additional evidence for the aforementioned biexcition formation mechanism in TMDs. Moreover, the formation of excited-state biexcitons are found to be strongly influenced by three important conditions: reduced dielectric screening, high density of trions, and high excitation power. By optimizing these three conditions, the emission of excited-state biexcitons could be triggered at room temperature in freestanding bilayer $MoSe_2$ samples,[57] and this can provide a platform to explore even higher-order many-body complexes in atomically thin semiconductors.

3.3. Diffusion Dynamics

The 2D or quasi-1D characteristics of excitons and trions can be validated by detecting their diffusion dynamics;[70–75] this is the time-resolved real-space distribution. Moreover, a detailed understanding of the diffusion dynamics in generated carriers is of great importance for photonic and optoelectronic applications.[28,76,77] By resolving the differential reflection signal in both time and space, the exciton lifetime (18 ps) and diffusion coefficient (15 ± 5 cm^2 s^{-1}) for monolayer WSe_2 could be determined. Other parameters characterizing the exciton dynamics such as the diffusion length (160 nm), the mean free time (0.24 ps), and the mean free length (17 nm) can be deduced based on these values.[78] For the transport dynamics, it was observed that the exciton and trion diffusion in TMDs are homogeneous along all directions around the excited point as shown in **Figure 5**a. Moreover, it was found that in monolayer WS_2, the transport dynamics of neutral excitons can be divided into three temperature ranges, where the diffusion of neutral excitons is governed by thermal activation (≤≈75 K), ionized impurity scattering (≈75 K ≤T ≤≈200 K), and LO phonon scattering (≥≈200 K). The trions have a diffusion length over 20 times longer than that of neutral excitons at very low temperatures (≤≈10 K).[70]

On the other hand, the exciton diffusion in BP is anisotropic resulting from its anisotropic lattice structure, where the mobility along the armchair direction is about 1 order of magnitude larger than that in the zigzag direction as illustrated in Figure 5b.[71] By following diffusion of photocarriers along these directions, the diffusion coefficients of 1300 and 80 cm^2 s^{-1} and diffusion lengths of about 4 and 1 μm along the armchair and zigzag directions were obtained, respectively. The anisotropic transport property can be mainly attributed to the anisotropic effective masses of electrons and holes. The effective masses of electrons with wavevectors along the armchair and zigzag directions are $0.0825m_0$ and $1.027m_0$, respectively. Hole effective masses of $0.0761m_0$ and $0.648m_0$ along the armchair and zigzag directions have also been observed, respectively.[71] The effective mass of carriers along the zigzag direction is about 10 times heavier than that along the armchair direction. Optically, both the absorption and emission features of BP are polarized, which have been validated by detecting the completely linearly polarized exciton and trion emissions by angle-resolved PL spectroscopy.[6]

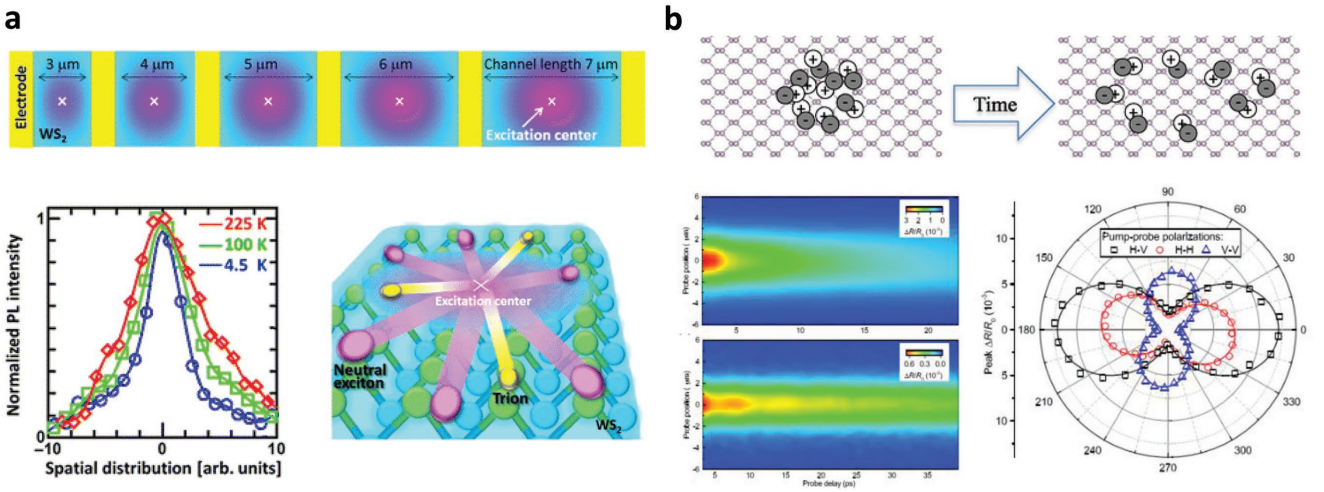

Figure 5. Diffusion dynamics of the many-body complexes. a) Isotropic diffusion of the exciton and trion in WS_2. Top: Exciton density profile in WS_2 for different channel lengths. Bottom left: Spatial profile of the neutral exciton density measured at different temperatures. Bottom right: Schematic plot showing the isotropic diffusion of the exciton and trion in WS_2. b) Anisotropic diffusion of the photocarriers in BP. Top: Schematic plots showing the anisotropic diffusion of the exciton in BP. Bottom left: Photocarrier diffusion along the armchair direction (upper) and the zigzag direction (under) in BP. Bottom right: Angular dependence of the differential reflection signal from BP. a) Reproduced with permission.[70] Copyright 2016, American Chemical Society. b) Reproduced with permission.[71] Copyright 2015, American Chemical Society.

4. Modulation of Material Properties

Due to the atomic thickness and extremely large surface area to volume ratio in the 2D limit, the property of many-body complexes can be modulated. Any coupling between 2D materials with external media can stimulate unique new phenomena and enable potential optoelectronic applications.

4.1. Bandgap Engineering

The first category of modulation can be summarized as the engineering of the intrinsic bandgap through temperature,[66,79,80] strain,[81–86] and heterostructure design,[87–96] etc. It has been known that monolayer TMDs are direct bandgap semiconductors in contrast to their indirect bandgap few-layer counterparts. Critically, in bilayer TMDs, the valleys Λ and K have very similar energy that can be tuned by temperature. As a result, bilayer MoS_2 can experience an indirect-to-direct bandgap transition at cryogenic temperatures, which significantly changes the photocarrier relaxation pathway in the PL process and leads to a fast increase of the PL intensity as the temperature decreases.[66] Moreover, this transition trend provides electrical tunability of exciton and trion dynamics in bilayer MoS_2 at low temperature, different from the case at room temperature as shown in **Figure 6**a. However, the PL intensity of bilayer $MoSe_2$ experiences an opposite trend (Figure 6b) to that of bilayer MoS_2 as temperature decreases despite their similar lattice structure. The movement of band valleys is sensitive to the change of lattice parameters a, u and c'. Hence, bilayer $MoSe_2$ and MoS_2 may undergo different lattice structure variations as a function of temperatures which requires further investigation.

Strain is another way that can be used to modulate the band structure and engineer the properties of 2D materials.[81–86] Specifically, the lattice constant and interlayer gap of 2D materials will change with strain and this leads to a direct change in the electronic band structure, and hence the energies of the conduction band minima and valence band maxima of the material. If the energy difference of the indirect and direct bandgaps is small, it is possible to achieve a crossover from one to the other using strain.[82] By applying uniaxial tensile strain of up to ≈2%, a drastic increase in PL intensity for multilayer WSe_2 was experimentally demonstrated, which is very similar to the phenomenon of indirect-to-direct bandgap transition. Based on DFT calculations, this is due to opposite shifts of the conduction band minima at the K and Σ points in the reciprocal space as shown in Figure 6c.[82] For anisotropic BP, the evolution of electronic properties under both uniaxial and biaxial strains (tensile and compressive) has been investigated by first-principles calculations.[85] By comparison, it was found that biaxial strain affects bandgap tuning more significantly than uniaxial strain alone. With zigzag tensile strain, the emergence of Dirac-like cones was observed in both monolayer and bilayer phosphorene (Figure 6d). Particularly, anisotropic Dirac-like dispersion was induced when appropriate armchair or biaxial compressive strain was applied to bilayer phosphorene.[85] Nevertheless, further experimental investigations of strain engineering on thin-layer phosphorene are required.

Heterostructures for band alignment involve two categories: lateral[89,91] or vertical[92,95] heterostructures. The availability of 2D materials with different working functions and band structures guarantees great potential for bandgap engineering through heterostructures.[89] The vertical heterostructure is constructed from two different TMD monolayers forming a type-II band alignment with bound electrons and holes localized in individual monolayers. Interlayer excitons have been observed in this kind of heterostructure from vertically stacked monolayer $MoSe_2$ and WSe_2 (Figure 6e) and this type of heterostructure

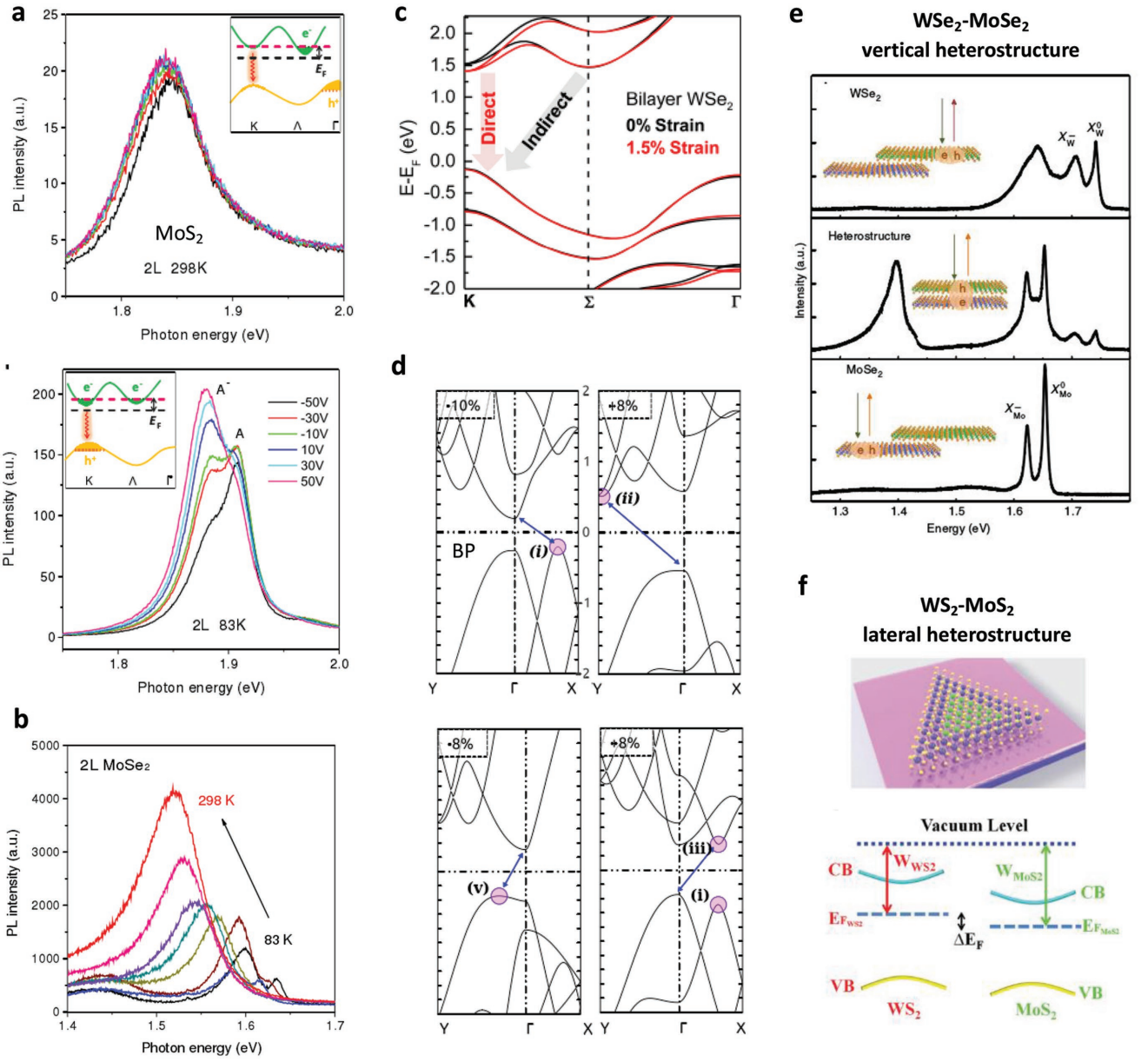

Figure 6. Bandgap engineering. a) Bandgap modulation of bilayer MoS_2 by temperature. Top: PL spectra of bilayer MoS_2 under different back gate voltages (from −50 to 50 V) at 298 K. Bottom: PL spectra of bilayer MoS_2 at 83 K. Insets show the schematic plot of the band structures modulation. b) Temperature-dependent PL spectra in bilayer $MoSe_2$. c) Band structure for bilayer WSe_2 with and without strain using HSE-DFT. d) Bandgap modulation of monolayer BP with uniaxial strain along the armchair direction (top) and the zigzag direction (bottom). e) Bandgap engineering with WSe_2–$MoSe_2$ vertical heterostructure. f) Bandgap engineering with WS_2–MoS_2 lateral heterostructure. Top: Schematic illustration of the heterostructure. Bottom: Schematic of band diagrams of type II MoS_2–WS_2 heterojunction. a) Reproduced with permission.[66] Copyright 2015, Wiley-VCH Verlag. c) Reproduced with permission.[82] Copyright 2014, American Chemical Society. d) Reproduced with permission.[85] Copyright 2015, AIP Publishing. e) Reproduced with permission.[95] Copyright 2015, Nature Publishing Group. f) Reproduced with permission.[89] Copyright 2015, Wiley-VCH Verlag.

has a much longer lifetime than intralayer excitons.[95] The PL intensity of interlayer excitons was enhanced under optical excitation resonance with intralayer excitons in isolated monolayers and this was a result of the interlayer charge transfer in the type-II band structure. The interlayer exciton energy could be tuned by applying a vertical gate voltage consistent with the permanent out-of-plane electric dipole nature of interlayer excitons.[95] Two different TMD monolayers could also form a lateral heterostructure by seamless stitching at the junction because of the same honeycomb lattice structure with closely matched lattice constants within the TMDs. Using the ambient pressure chemical vapor deposition (APCVD) process, an in-plane WS_2/MoS_2 heterostructure was formed with a type-II heterojunction.[89] The photon excited electrons and holes are confined to locate at two separate materials forming an inherent potential in the heterojunction (Figure 6f).

4.2. Defect Engineering

Defect engineering is another aspect of modulation that changes the internal structure of 2D semiconductors.[56,97–105] Defects in semiconductors, such as vacancies and interstitials, can strongly influence transport and optical properties of the host material and such interactions become stronger in lower dimensional materials due to tighter localization of the electron wave function.[106] More specifically, defects can introduce extra electronic states in the bandgap and significantly influence the carrier transport in semiconductors. Deep insight into the functionalities of defects and precise control of them provide the possibility of tailoring the optical properties of 2D semiconductors that can lead to new applications.

A strong PL enhancement (three orders) has been observed in monolayer MoS_2 cracks after high-temperature annealing.[98] The PL enhancement resulted from the oxygen absorption from air. This process could also be realized through defect engineering and oxygen bonding under plasma irradiation as shown in **Figure 7**a, where more reactive conditions were provided. The mechanism of such huge PL enhancement can be explained by 1) the conversion from trion to exciton due to the oxygen chemical adsorption induced heavy p doping; 2) the suppression of nonradiative recombination of excitons at defect sites.[98] The oxygen molecule was found chemically adsorbed on a S vacancy instead of physically adsorbed on the surface. As a result, a much more effective charge transfer was provided by the chemically adsorbed oxygen. When phosphorene is subjected to oxygen plasma, its internal structure can be engineered in two aspects.[99] A stable and uniform P_xO_y layer can be generated on the top of phosphorene layers (Figure 7b, left). By carefully controlling the oxygen flow rate, plasma generation power, and etching time, a high-quality monolayer BP could be fabricated with prolonged living time because of the well-protected surface induced by the P_xO_y layer. Additionally, through controllable etching with oxygen plasma, oxygen defects could also be introduced in phosphorene. Contrary to the PL enhancement effect in TMDs, the oxygen defect in phosphorene gave rise to two strong PL peaks at 780 and 915 nm, respectively (Figure 7b, right). The defect nature of these two peaks was confirmed by power-dependent PL measurements. These two peaks have been attributed to the emissions from excitons localized onto the bridge-type defect points (horizontal and diagonal bridges); this has been predicted to create energy levels in the bandgap by numerical simulations as indicated by the energy diagrams shown in Figure 7c.[104] These defect states serve as recombination centers to generate photon emissions. Due to the broad peak width, there might be contributions from other kinds of defects such as dangling oxygen, interstitial oxygen, physisorbed oxygen, water, etc.[104] In addition, the emission from oxygen defects in phosphorene has been clearly observed at room temperature that could be due to their large trapping energy.[99] In contrast, the localized exciton emissions for monolayer TMDs are observable

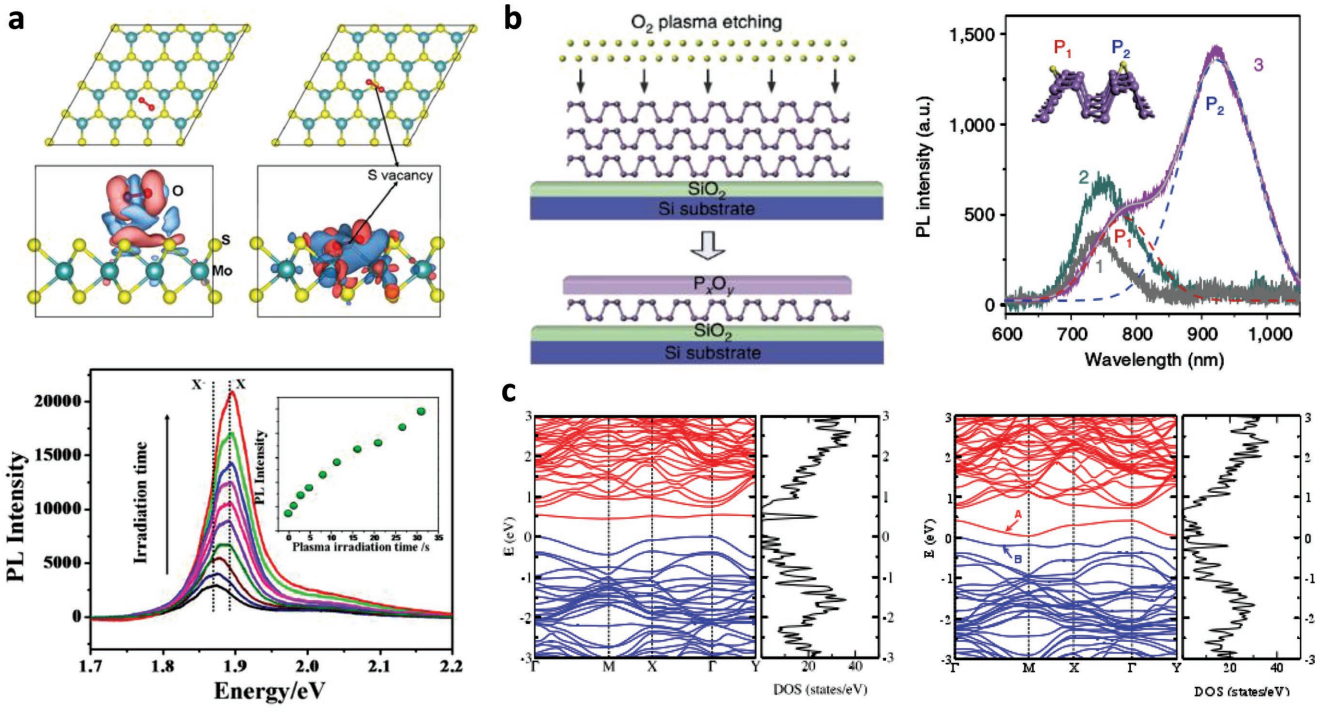

Figure 7. Defect engineering. a) Oxygen plasma irradiation on MoS_2. Top left: Charge density difference of an O_2 molecule physisorbed on perfect monolayer MoS_2. Top right: Charge density difference of an O_2 molecule chemisorbed on defective monolayer MoS_2 containing a monosulfur vacancy. Bottom: PL spectra of monolayer MoS_2 after oxygen plasma irradiation with different durations. b) Oxygen plasma etching on BP. Top left: Schematic illustration of the oxygen plasma etching process. Top right: PL spectra of monolayer phosphorene samples with (curves 1 and 2) and without (curve 3) oxygen defect. Inset shows the schematic plot of two different oxygen defects. c) The band structures of oxygen bridged monolayer BP. Left: Horizontal oxygen bridged. Right: Diagonal oxygen bridged. a) Reproduced with permission.[98] Copyright 2014, American Chemical Society. b) Reproduced with permission.[99] Copyright 2016, Nature Publishing Group. c) Reproduced with permission.[104] Copyright 2015, American Physical Society.

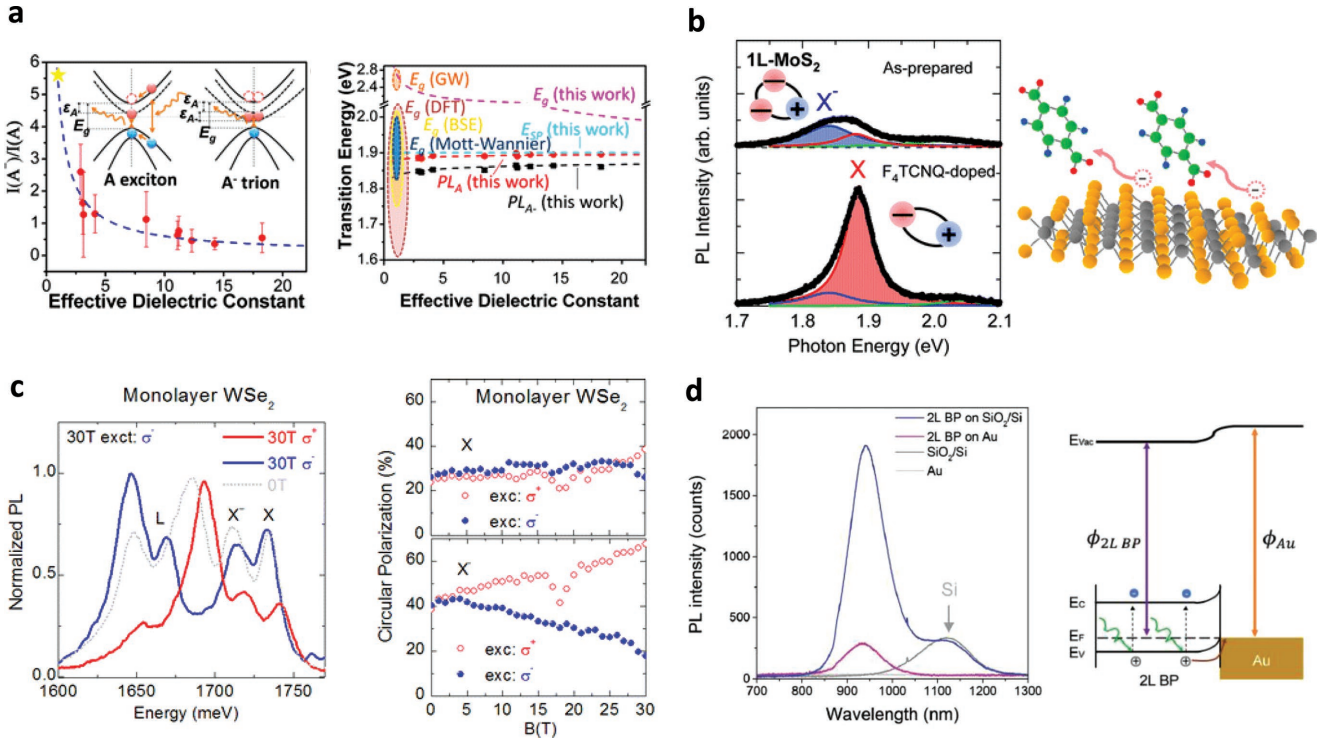

Figure 8. Environmental engineering. a) Modulation with screening effect. Left: The A^-/A intensity ratio as a function of the effective dielectric constant. Right: PL peak energies of the exciton and trion as a function of the effective dielectric constant. b) Modulation with chemical doping. Left: PL spectral for as-prepared and F_4TCNQ-doped monolayer MoS_2. Right: Schematic illustration of the chemical doping process. c) Modulation with external magnetic field. Left: Circular polarization of the PL spectra for monolayer WSe_2 in high magnetic fields. Right: Degree of circular polarization of the exciton and trion. d) Modulation with quenching effect. Left: Measured PL spectra from the bilayer BP on Au and SiO_2 substrates. Right: Schematic illustration of the mechanism of PL quenching in the phosphorene–gold hybrid system. a) Reproduced with permission.[19] Copyright 2014, American Chemical Society. b) Reproduced with permission.[20] Copyright 2013, American Chemical Society. c) Reproduced with permission.[112] Copyright 2015, American Chemical Society. d) Reproduced with permission.[114] Copyright 2015, Royal Society of Chemistry.

only at cryogenic temperatures and in the presence of N_2 gas molecules.[56]

4.3. Environmental Engineering

Other works are categorized toward environmental engineering modulations in the external environment within the vicinity of 2D layers, such as dielectric screening,[19,107,108] chemical doping,[20,109–111] magnetic field,[112] and substrates.[113,114] Environmental dielectrics have been found to strongly influence the Coulomb interactions in low dimensional materials.[115,116] Many-body complexes originating from strong electron–hole Coulomb interactions are strongly coupled with the dielectric properties of surrounding materials.[19] This would result in changes in their optical properties which can be reflected by the optical transitions of excitons and trions. The extrinsic influence of the dielectric constant on the environment and exciton behaviors has been demonstrated on monolayer MoS_2 using nonionic organic solvents as the environmental dielectrics.[19] Up to 40 meV of blueshifts in the PL peak energies as a function of the dielectric constant was observed. The shifts were attributed to the increase in binding energies of excitons and trions as a result of reduced dielectric screening. Moreover, the ratio of the PL intensity between trions and excitons increased as the dielectric constant decreased (**Figure 8**a), indicating the transition from excitons to trions as the dielectric screening weakened. Therefore, the higher-order many-body complexes such as biexcitons could be expected in an environment with much weaker dielectric screening such as freestanding structures.

The interplay between the excitons and charge carriers leads to the formation of many-body complexes such as trions and biexcitons in 2D semiconductors. Control of the carrier density by gate doping provides one way to modulate their properties.[11,12] Chemical doping is another way to control the carrier density.[20] The charge transfer between the dopant molecules and the 2D materials is expected to induce a shift in the Fermi level and to enable large modulations of the optical and electrical properties.[20] By changing the type of dopants and carrier densities, switching of the PL emissions between excitons and trions in monolayer MoS_2 has been demonstrated, similar to gate doping–induced modulation. The p-type dopants with high electron affinity contribute to the transition from trion to exciton emissions and can substantially enhance the PL intensity of monolayer MoS_2 (Figure 8b). However, the PL intensity reduced because of the adsorption of n-type dopants and this was due to the transition from exciton to trion emissions.

In monolayer TMDs, the valley and spin polarization can be manipulated by an external magnetic field since the carriers in the +K and –K valleys are subjected to opposite Berry curvatures,

and these act as an effective magnetic field in the momentum space.[36] Many-body complexes also possess a valley degree of freedom because of the localization of the constituent electrons and holes in the +K and −K valleys. In high magnetic fields up to $B = 65$ T, the exciton and trion emissions of monolayer WSe_2 exhibit a splitting that originates from the magnetic field induced lifting of the valley degeneracy.[112] The magnetic field was also found to significantly influence the valley polarization of trions depending on the circular polarization of the excitation light but have little effect on the valley polarization of excitons (Figure 8c). Notably, the PL peak is around 1.69 eV in Figure 8c which was not analyzed further in the work;[112] however, it was proved to be the emission of biexcitons in later work.[14] The strong polarization dependence of this peak under high magnetic fields may help distinguish the excited-state and ground-state biexciton in the future since the two biexciton states have different spins and probably act differently under out-of-plane magnetic fields.[16]

The commonly used substrates for 2D materials (such as SiO_2, BN, sapphire, and polymer) are known as dielectric substrates, which have strong influence on both the PL intensity and peak energy of 2D semiconductors due to the aforementioned dielectric screening effect. The quenching effect is also important for 2D semiconductors on a conducting substrate such as Au or Cu, in which interfacial charge transfer plays a key role.[92,117] Highly anisotropic and layer-dependent PL quenching has been observed in a phosphorene–gold hybrid system (Figure 8d) and this was due to the highly anisotropic/layer-dependent interfacial charge transfer in the system.[114] The charge transfer in a phosphorene–gold hybrid system was probed by PL spectroscopy. At the same time, the strong layer-dependent surface potential of mono- and few-layer phosphorene on a gold substrate was directly measured by Kelvin probe force microscopy.[114]

5. Optoelectronic Applications

The strong excitonic effect in 2D semiconductors allows their utility in optical and optoelectronic applications.[118–130] The recombination of electrons and holes from excitons and trions, etc., results in photon emissions from semiconductors. When the photoexcited electrons and holes are separated from the conduction band and valence band and driven to electrodes, a photocurrent can be generated. The former phenomenon is the working principle of luminescence devices such as excitonic lasers[120–123] and light-emitting diodes (LEDs),[118,125] and the latter is the basis of photoelectric devices such as solar cells[124] and photodetectors.[126–128] Here, we briefly introduce several representative optoelectronic applications based on 2D semiconductors.

5.1. Luminescence Devices

The tightly bound excitons and trions in 2D TMDs allow for the long-lived population inversion required to achieve optical gain and to possibly stimulate emissions. By integrating the monolayer WS_2 into a strong-feedback photonic cavity, an ultralow-threshold (5–8 MW cm^{-2}) monolayer excitonic laser was demonstrated (**Figure 9**a).[122] The monolayer WS_2 was embedded between two dielectric layers in a microdisk resonator that provided strong optical confinement and large modal gain. The cavity resonance was designed to overlap with the gain spectrum of the monolayer WS_2 and the electric field polarized in the plane of the TMD monolayer efficiently coupled with the in-plane dipoles of the excitons.[122] Moreover, gain–cavity coupling could also be achieved through the combination of monolayer TMDs with a photonic crystal (Figure 9b), in which the resonant mode was carefully designed to match the PL emission of monolayer TMDs. A continuous-wave nanolaser was achieved with an optical pumping threshold as low as 27 nW (≈1 W cm^{-2}) at 130 K.[123] Recently, strong exciton–photon coupling was demonstrated by placing a monolayer WS_2 or WSe_2 over a photonic crystal made of a silicon-nitride (SiN) grating, forming microcavity exciton–polaritons that offer future prospects for the development of room-temperature polariton lasers.[131] Polaritons could be observed at room temperature for WS_2 and up to 110 K for WSe_2; additionally, the nonradiative decay due to dark excitons is strongly suppressed because of polariton enhanced radiative decay.

It is known that PL arises from the recombination of photoexcited electrons and holes, and similarly, electroluminescence (EL) originates from the recombination of electric-injected electrons and holes. EL provides another approach for the design of luminescence devices. By combining monolayer WSe_2 with a p–n junction architecture using electrostatic doping, a tunable excitonic LED has been demonstrated (Figure 9c).[124,125] The injected electrons and holes were found to form excitons or trions prior to recombining radiatively and this was due to the similarity between the EL and PL spectra. By increasing the bias, the EL from impurity-bound charged and neutral excitons could be modulated.[125] The LED structure shown in Figure 9c belongs to the lateral p–n junction strategy, where the active region is limited to a narrow depletion area. Later, vertical van der Waals heterojunctions were proposed to effectively enlarge the active region of the whole overlapping area.[132] By stacking metallic graphene, insulating hexagonal boron nitride, and various semiconducting monolayers into complex but carefully designed sequences, the extrinsic quantum efficiency could be further improved to nearly 10% with tunable frequencies of emissions.[96] The carrier-to-exciton conversion efficiency is an important issue that should be addressed for the EL process. The previously reported vertically integrated devices typically require large current densities (at the range of several μA $μm^{-2}$) to trigger light emission due to current leakage. However, a recent study showed a field emission tunnel diode with an extremely low threshold current density of 4 pA $μm^{-2}$; this was based on a metal–insulator–semiconductor (MIS) van der Waals heterostack consisting of few-layer graphene, hBN and monolayer WS_2, and the carrier-to-exciton conversion efficiency was significantly improved.[133] For more novel luminescence devices that are constructed based on 2D semiconductors, readers are referred to the recent reviews.[35,134]

5.2. Photoelectric Devices

In addition to light-emitting devices, p–n diodes are also suitable for solar energy conversion devices when reversing the

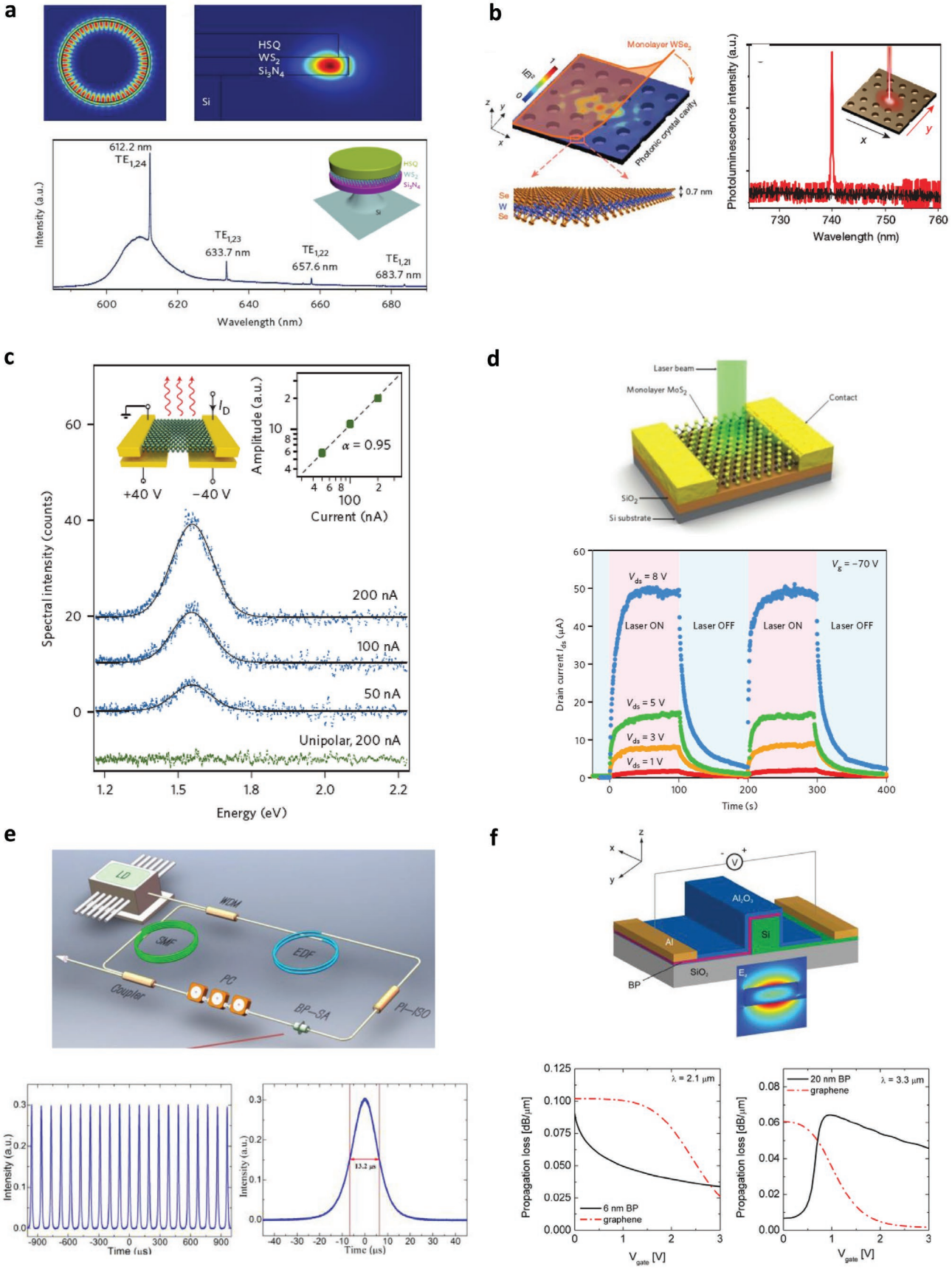

process of EL in Figure 9c. Under optical illumination, electrons and holes are generated in the conduction band and the valence band from the channel material, respectively. When biased in a p–n diode configuration, the electrons and holes are forced to separate by the built-in electric field and will form a current flow and voltage to the external load. The light–power conversion efficiency of an early reported 2D semiconductor photovoltaic device was about 0.5%,[124] and the gap between the gates should be narrow (≈500 nm) in the lateral p–n junctions. In order to increase the photoelectric conversion efficiency, it is required that more electrons and holes could reach the electrodes before the recombination of excitons. The strategy could be achieved through developing vertical heterojunctions by transferring large-scale monolayer MoS_2 onto a p-Si substrate, in which a built-in electric field near the interface between MoS_2 and p-Si was formed and a power conversion efficiency of 5.23% has been achieved.[135] The power conversion efficiency could be further improved by using graphene as a charge collecting electrode. Highly efficient photocurrent generation from vertically stacked graphene–MoS_2–graphene heterostructures have been reported with a maximum external quantum efficiency of 55% and an internal quantum efficiency up to 85%.[136] A recent study also showed that a graphene/WSe_2/graphene sandwiched structure can achieve efficient photoinduced carrier separation in an extremely short time period (≈5.5 ps).[93] This high photodetection efficiency and picosecond photoresponse makes it particularly suitable for the application of photodetectors.

Photodetectors work on a similar principle to solar cells and this is based on an internal photoelectric effect. Upon illumination, the excitons/trions are generated and electron–hole pairs are separated in 2D semiconductors generating a measurable electrical signal (Figure 9d). 2D TMDs show great potential for photodetector applications beyond graphene due to their low dark current, large bandgap, and relative long carrier lifetime, in addition to ultrahigh sensitivity and fast photoresponsivity.[137,138] With gold nanoparticles (AuNPs) embedded in the gate dielectric of a WS_2 phototransistor, an ultralow dark current of 10^{-11} A, a high photoresponsivity of 1090 A W^{-1}, and a detectivity of 3.5×10^{11} Jones were achieved under a zero gate voltage and a small source/drain bias.[137] In another work, an ultrasensitive detector comprising solely of 2D-TMD materials enabled by bandgap engineering in the out-of-plane direction through chemical surface doping was reported; the photoexcited carriers were separated efficiently; and a photoconductive gain of $>10^5$ electrons per photon, external quantum efficiency greater than 10%, and a responsivity of 7×10^4 A W^{-1} were measured.[138]

Compared to TMDs, BP has higher carrier mobility and has direct bandgap behavior from bulk (0.3 eV) to monolayer (2.0 eV); this feature enables the construction of more effective and efficient broadband photodetectors. A high photoresponsivity of about 7×10^6 A W^{-1} at 20 K and 4.3×10^6 A W^{-1} at 300 K has been achieved for a BP-based photodetector in the wavelength range from 400 to 900 nm, respectively.[139] More recently, a study showed that a vertical electric field can be used to dynamically extend the photoresponse beyond the cutoff wavelength (from 3.7 to 7.7 μm) of pristine BP in a 5 nm thick BP photodetector based on an hBN/BP/hBN heterostructure.[140] The intrinsic bandgaps as well as strong light absorption of up to 30% makes thin-layer TMDs and BP promising candidates for highly efficient absorption layers for solar cells and photodetectors. More importantly, the tunable bandgap of TMDs and BP range from the ultraviolet region to the near-infrared region, and this makes them promising building blocks for photodetectors with a multispectral response. Note that two recent review papers provide detailed discussions on 2D TMD- and BP-based photovoltaic devices[141] and photodetectors,[142] respectively.

5.3. Optical Modulators

The diverse electronic structures, strong excitonic effects, and controllable optoelectronic properties make 2D materials suitable candidates for optical modulation, such as optical limiters, mode lockers, and Q-switchers.[124,143] Benefitted from their broadband optical response and ultrafast carrier dynamics, 2D materials have emerged as promising saturable absorbers for ultrashort pulse generations.[37] Graphene was first shown to exhibit broadband optical saturable absorption and has been applied successfully in passive mode locking or Q-switching of both fiber and solid-state lasers.[130,144] But the absence of bandgap and the low absorption coefficient of graphene restrain its applications in situations where strong light–matter interactions are required. Lately, TMDs were found to have strong light–matter interactions and a unique absorption property, and they have received extensive investigations as effective saturable absorbers for pulsed laser applications; for example, a few-layer MoS_2-based mode locker for a ytterbium-doped fiber laser could generate stable laser pulses centered at 1054.3 nm, with a 3 dB spectral bandwidth of 2.7 nm and a pulse duration of 800 ps.[143] However, a blank space between the visible and mid-infrared regions was absent until the discovery of BP as a saturable absorber (Figure 9e),[145] where the passive

Figure 9. Optoelectronic applications. a) Excitonic laser. Top: Top view and cross-sectional view of the simulated electric field distribution of the $TE_{1,24}$ resonance. Bottom: PL spectrum of the device when the pump intensity is above lasing threshold. Inset shows the schematic plot of the microdisk resonator. b) Nanocavity laser. Left: Schematic illustration of the hybrid monolayer WSe_2–PCC nanolaser device. Right: Polarization-resolved PL spectrum of the device. c) LED/solar cell. Inset: Schematic illustration of the device operation as a LED. d) Photodetector. Top: Schematic illustration of the monolayer MoS_2 photodetector. Bottom: Time-resolved photoresponse of the device under different bias voltages. e) BP-SA based Q-switching erbium-doped fiber laser. Top: Schematic illustration of the experimental setup. Bottom: Output pulse train (left) and single pulse profile (right) of Q-switching pulse emitted from the BP-SA-based fiber laser. f) BP-assisted, traveling-wave electroabsorption modulator. Top: Schematic illustration of the modulator structure. Bottom: Waveguide loss for modulator integrated with 6 nm BP (left) and 20 nm BP (right) active layer, respectively. a) Reproduced with permission.[122] Copyright 2015, Nature Publishing Group. b) Reproduced with permission.[123] Copyright 2015, Nature Publishing Group. c) Reproduced with permission.[124] Copyright 2014, Nature Publishing Group. d) Reproduced with permission.[127] Copyright 2013, Nature Publishing Group. e) Reproduced with permission.[145] Copyright 2015, Optical Society of America. f) Reproduced with permission.[148] Copyright 2016, American Chemical Society.

Q-switching (with a maximum pulse energy of 94.3 nJ) or the passive mode-locking operation (with a pulse duration down to 946 fs) could be obtained by incorporating the BP-based SA device into the all-fiber Erbium-doped fiber laser cavity. A more recent study showed that a BP-based mode-locked Er:ZBLAN fiber laser could reach a wavelength of 2.8 µm with a maximum average output power of 613 mW, a repetition rate of 24 MHz, and a pulse duration of 42 ps. This was done by transferring the mechanically exfoliated BP onto a gold-coated saturable absorbing mirror.[146] Such optical modulators are known as all-optical modulators, for which the modulation was done directly in an optical fiber or other waveguide structure.

Because the optoelectronic properties of 2D semiconductors are extremely sensitive to external stimuli, they can be modified by external fields such as electric, thermal, magnetic, and acoustic fields. Modulation devices based on these principles are classified as the electro-optic, thermo-optic, magneto-optic, and acousto-optic modulators. For example, a strong second-harmonic generation (SHG) nonlinear optical response was triggered in a monolayer WSe_2 under a back gate field and this could not be observed in bilayer WSe_2 because of inversion symmetry.[147] For few-layer BP, the absorption band edge could be modulated to red-, blue-, or bidirectional shift by applying an out-of-plane electric field, resulting from the interplay between the field-induced quantum-confined Franz–Keldysh effect (QCFK) and the Pauli-blocked Burstein–Moss shift (BMS),[148,149] making it a versatile electro-optic material for mid-infrared modulations; the structure of the modulator is shown in Figure 9f, which consists of a BP thin film overlaid on top of a Si nanowire separated by a 7 nm Al_2O_3 spacer. Through measurements of the waveguide loss factor for a modulator with different BP thickness under different gate voltages, it was found that a 20 nm BP-assisted modulator only requires $P = 0.59$ V of power consumption and this is a 62% reduction compared to the use of the BMS effect in its graphene counterpart ($P = 1.56$ V). More approaches have been reported recently in addition to electric field modulation, such as the magnetic control of the optical transport properties in monolayer WSe_2[150] and the strain engineering of optical properties in BP; moreover, a remarkable shift of the optical absorption band edge of up to ≈0.7 eV between the regions under tensile and compressive stress has been observed.[84] By using optical resonance structures such as plasmonic structures and optical cavities, the light–matter interactions in 2D semiconductors can be further improved or manipulated.[151] So far, optical modulators based on 2D materials have made great progress in many aspects covering the visible to infrared regions through various novel functional configurations.[37,152]

6. Conclusions and Prospects

Many-body complexes, such as excitons, trions, and biexcitons, are elementary quasiparticles arising from the excitonic effect and they play a key role in optoelectronic applications of 2D semiconductors, from LED and solar cells to photodetectors and optical modulators. Characterization and control of many-body complexes has become a reality due to enhanced binding energies in the 2D limit. At the same time, the sensitivity of these complexes to external stimuli can offer unprecedented tunability and diversifies the applications of 2D semiconductors. It is essential to fully realize these excitonic structures before turning the proof-of-concept devices into practical uses.

Despite the substantial progress so far, there are still significant challenges remaining. Significant theoretical investigations are needed as there are conflicts on the exact formation mechanism and the binding energies of many-body complexes. Additionally, more experiments are necessary to characterize the different complexes and validate the theoretical models. In addition to excitons, trions, and biexcitons, higher-order excitonic states or localized states are yet to receive substantial attention. The diffusion dynamics of the many-body complexes in various circumstances are still underexplored because the optoelectronic devices may work in complicated conditions. Improving the quantum efficiency in current materials is a key problem to enhancing device performance. Besides TMDs and BP, new materials with higher conversion efficiency or other unique properties (such as perovskite and antimonene) may serve as new building blocks for optoelectronic devices. The study of many-body complexes in these materials or their heterostructures is also desirable in the future. Lastly, as the exciton, trion, and biexciton states have different symmetries and dynamically controllable valley and spins, it is of great interest to apply them in novel applications such as single photon sources for future quantum communications and quantum cryptography.

Acknowledgements

The authors acknowledge financial support from the National Natural Science Foundation of China (Grant No. 61435010), the Australian Research Council (Grant No. DE140100805), and China Postdoctoral Science Foundation (Grant No. 2017M622764).

Conflict of Interest

The authors declare no conflict of interest.

Keywords

2D materials, biexcitons, excitons, optoelectronic applications, trions

Received: November 28, 2017
Revised: June 10, 2018
Published online: August 20, 2018

[1] K. S. Novoselov, A. K. Geim, S. V. Morozov, D. Jiang, Y. Zhang, S. V. Dubonos, I. V. Grigorieva, A. A. Firsov, *Science* **2004**, *306*, 666.
[2] C. Tan, X. Cao, X.-J. Wu, Q. He, J. Yang, X. Zhang, J. Chen, W. Zhao, S. Han, G.-H. Nam, M. Sindoro, H. Zhang, *Chem. Rev.* **2017**, *117*, 6225.
[3] Q. H. Wang, K. Kalantar-Zadeh, A. Kis, J. N. Coleman, M. S. Strano, *Nat. Nanotechnol.* **2012**, *7*, 699.
[4] K. F. Mak, J. Shan, *Nat. Photonics* **2016**, *10*, 216.
[5] A. Carvalho, M. Wang, X. Zhu, A. S. Rodin, H. Su, A. H. Castro Neto, *Nat. Rev. Mater.* **2016**, *1*, 16061.

[6] J. Lu, J. Yang, A. Carvalho, H. Liu, Y. Lu, C. H. Sow, *Acc. Chem. Res.* **2016**, *49*, 1806.
[7] A. Splendiani, L. Sun, Y. Zhang, T. Li, J. Kim, C.-Y. Chim, G. Galli, F. Wang, *Nano Lett.* **2010**, *10*, 1271.
[8] R. Roldán, J. A. Silva-Guillén, M. P. López-Sancho, F. Guinea, E. Cappelluti, P. Ordejón, *Ann. Phys. (Berlin)* **2014**, *526*, 347.
[9] S. Zhang, J. Yang, R. Xu, F. Wang, W. Li, M. Ghufran, Y.-W. Zhang, Z. Yu, G. Zhang, Q. Qin, Y. Lu, *ACS Nano* **2014**, *8*, 9590.
[10] J. Qiao, X. Kong, Z.-X. Hu, F. Yang, W. Ji, *Nat. Commun.* **2014**, *5*, 4475.
[11] J. S. Ross, S. Wu, H. Yu, N. J. Ghimire, A. M. Jones, G. Aivazian, J. Yan, D. G. Mandrus, D. Xiao, W. Yao, X. Xu, *Nat. Commun.* **2013**, *4*, 1474.
[12] K. F. Mak, K. He, C. Lee, G. H. Lee, J. Hone, T. F. Heinz, J. Shan, *Nat. Mater.* **2012**, *12*, 207.
[13] J. Shang, X. Shen, C. Cong, N. Peimyoo, B. Cao, M. Eginligil, T. Yu, *ACS Nano* **2015**, *9*, 647.
[14] Y. You, X.-X. Zhang, T. C. Berkelbach, M. S. Hybertsen, D. R. Reichman, T. F. Heinz, *Nat. Phys.* **2015**, *11*, 477.
[15] I. Kylänpää, H.-P. Komsa, *Phys. Rev. B* **2015**, *92*, 205418.
[16] D. K. Zhang, D. W. Kidd, K. Varga, *Nano Lett.* **2015**, *15*, 7002.
[17] R. Xu, S. Zhang, F. Wang, J. Yang, Z. Wang, J. Pei, Y. W. Myint, B. Xing, Z. Yu, L. Fu, Q. Qin, Y. Lu, *ACS Nano* **2016**, *10*, 2046.
[18] A. Chernikov, T. C. Berkelbach, H. M. Hill, A. Rigosi, Y. Li, O. B. Aslan, D. R. Reichman, M. S. Hybertsen, T. F. Heinz, *Phys. Rev. Lett.* **2014**, *113*, 076802.
[19] Y. Lin, X. Ling, L. Yu, S. Huang, A. L. Hsu, Y.-H. Lee, J. Kong, M. S. Dresselhaus, T. Palacios, *Nano Lett.* **2014**, *14*, 5569.
[20] S. Mouri, Y. Miyauchi, K. Matsuda, *Nano Lett.* **2013**, *13*, 5944.
[21] T. C. Berkelbach, M. S. Hybertsen, D. R. Reichman, *Phys. Rev. B* **2013**, *88*, 045318.
[22] A. Chaves, M. Z. Mayers, F. M. Peeters, D. R. Reichman, *Phys. Rev. B* **2016**, *93*, 115314.
[23] A. S. Rodin, A. Carvalho, A. H. Castro Neto, *Phys. Rev. B* **2014**, *90*, 075429.
[24] M. Z. Mayers, T. C. Berkelbach, M. S. Hybertsen, D. R. Reichman, *Phys. Rev. B* **2015**, *92*, 161404.
[25] Z. Ye, T. Cao, K. O'Brien, H. Zhu, X. Yin, Y. Wang, S. G. Louie, X. Zhang, *Nature* **2014**, *513*, 214.
[26] H. S. Lee, M. S. Kim, H. Kim, Y. H. Lee, *Phys. Rev. B* **2016**, *93*, 140409.
[27] J. Yang, T. Lü, Y. W. Myint, J. Pei, D. Macdonald, J.-C. Zheng, Y. Lu, *ACS Nano* **2015**, *9*, 6603.
[28] D. Kozawa, R. Kumar, A. Carvalho, K. Kumar Amara, W. Zhao, S. Wang, M. Toh, R. M. Ribeiro, A. H. Castro Neto, K. Matsuda, G. Eda, *Nat. Commun.* **2014**, *5*, 4543.
[29] J. Yang, R. Xu, J. Pei, Y. W. Myint, F. Wang, Z. Wang, S. Zhang, Z. Yu, Y. Lu, *Light: Sci. Appl.* **2015**, *4*, e312.
[30] K. He, N. Kumar, L. Zhao, Z. Wang, K. F. Mak, H. Zhao, J. Shan, *Phys. Rev. Lett.* **2014**, *113*, 026803.
[31] S. Z. Butler, S. M. Hollen, L. Cao, Y. Cui, J. A. Gupta, H. R. Gutiérrez, T. F. Heinz, S. S. Hong, J. Huang, A. F. Ismach, E. Johnston-Halperin, M. Kuno, V. V. Plashnitsa, R. D. Robinson, R. S. Ruoff, S. Salahuddin, J. Shan, L. Shi, M. G. Spencer, M. Terrones, W. Windl, J. E. Goldberger, *ACS Nano* **2013**, *7*, 2898.
[32] A. Gupta, T. Sakthivel, S. Seal, *Prog. Mater. Sci.* **2015**, *73*, 44.
[33] A. J. Mannix, B. Kiraly, M. C. Hersam, N. P. Guisinger, *Nat. Rev. Chem.* **2017**, *1*, 0014.
[34] J. Yu, J. Li, W. Zhang, H. Chang, *Chem. Sci.* **2015**, *6*, 6705.
[35] Y. Liu, N. O. Weiss, X. Duan, H.-C. Cheng, Y. Huang, X. Duan, *Nat. Rev. Mater.* **2016**, *1*, 16042.
[36] J. R. Schaibley, H. Yu, G. Clark, P. Rivera, J. S. Ross, K. L. Seyler, W. Yao, X. Xu, *Nat. Rev. Mater.* **2016**, *1*, 16055.
[37] S. Yu, X. Wu, Y. Wang, X. Guo, L. Tong, *Adv. Mater.* **2017**, *29*, 1606128.
[38] J. K. Ellis, M. J. Lucero, G. E. Scuseria, *Appl. Phys. Lett.* **2011**, *99*, 261908.
[39] V. Tran, R. Soklaski, Y. Liang, L. Yang, *Phys. Rev. B* **2014**, *89*, 235319.
[40] T. Cheiwchanchamnangij, W. R. L. Lambrecht, *Phys. Rev. B* **2012**, *85*, 205302.
[41] W. Qianwen, W. Ping, C. Gengyu, H. Min, *J. Phys. D: Appl. Phys.* **2013**, *46*, 505308.
[42] W. Zhao, R. M. Ribeiro, M. Toh, A. Carvalho, C. Kloc, A. H. Castro Neto, G. Eda, *Nano Lett.* **2013**, *13*, 5627.
[43] A. Ramasubramaniam, *Phys. Rev. B* **2012**, *86*, 115409.
[44] E. J. Sie, A. J. Frenzel, Y.-H. Lee, J. Kong, N. Gedik, *Phys. Rev. B* **2015**, *92*, 125417.
[45] A. Thilagam, *J. Appl. Phys.* **2014**, *116*, 053523.
[46] K. A. Velizhanin, A. Saxena, *Phys. Rev. B* **2015**, *92*, 195305.
[47] H. Wang, C. Zhang, W. Chan, C. Manolatou, S. Tiwari, F. Rana, *Phys. Rev. B* **2016**, *93*, 045407.
[48] X. Li, L. Tao, Z. Chen, H. Fang, X. Li, X. Wang, J.-B. Xu, H. Zhu, *Appl. Phys. Rev.* **2017**, *4*, 021306.
[49] X. Li, L. Wei, R. H. Poelma, S. Vollebregt, J. Wei, H. P. Urbach, P. M. Sarro, G. Q. Zhang, *Sci. Rep.* **2016**, *6*, 25348.
[50] M. S. Kim, S. J. Yun, Y. Lee, C. Seo, G. H. Han, K. K. Kim, Y. H. Lee, J. Kim, *ACS Nano* **2016**, *10*, 2399.
[51] C. Mai, A. Barrette, Y. Yu, Y. G. Semenov, K. W. Kim, L. Cao, K. Gundogdu, *Nano Lett.* **2014**, *14*, 202.
[52] G. Plechinger, P. Nagler, J. Kraus, N. Paradiso, C. Strunk, C. Schüller, T. Korn, *Phys. Status Solidi RRL* **2015**, *9*, 457.
[53] H. Rodriguez Gutierrez, N. Perea-López, A. Elías, A. Berkdemir, B. Wang, R. Lv, F. López-Urías, V. Crespi, H. Terrones, M. Terrones, *Nano Lett.* **2014**, *13*, 3447.
[54] T. Yan, X. Qiao, X. Liu, P. Tan, X. Zhang, *Appl. Phys. Lett.* **2014**, *105*, 101901.
[55] Y.-M. He, O. Iff, N. Lundt, V. Baumann, M. Davanco, K. Srinivasan, S. Höfling, C. Schneider, *Nat. Commun.* **2016**, *7*, 13409.
[56] S. Tongay, J. Suh, C. Ataca, W. Fan, A. Luce, J. S. Kang, J. Liu, C. Ko, R. Raghunathanan, J. Zhou, F. Ogletree, J. Li, J. C. Grossman, J. Wu, *Sci. Rep.* **2013**, *3*, 2657.
[57] J. Pei, J. Yang, X. Wang, F. Wang, S. Mokkapati, T. Lü, J.-C. Zheng, Q. Qin, D. Neshev, H. H. Tan, C. Jagadish, Y. Lu, *ACS Nano* **2017**, *11*, 7468.
[58] X. Xu, W. Yao, D. Xiao, T. F. Heinz, *Nat. Phys.* **2014**, *10*, 343.
[59] J. A. Schuller, S. Karaveli, T. Schiros, K. He, S. Yang, I. Kymissis, J. Shan, R. Zia, *Nat. Nanotechnol.* **2013**, *8*, 271.
[60] A. R. Klots, A. K. M. Newaz, B. Wang, D. Prasai, H. Krzyzanowska, J. Lin, D. Caudel, N. J. Ghimire, J. Yan, B. L. Ivanov, K. A. Velizhanin, A. Burger, D. G. Mandrus, N. H. Tolk, S. T. Pantelides, K. I. Bolotin, *Sci. Rep.* **2014**, *4*, 6608.
[61] M. M. Ugeda, A. J. Bradley, S.-F. Shi, F. H. da Jornada, Y. Zhang, D. Y. Qiu, W. Ruan, S.-K. Mo, Z. Hussain, Z.-X. Shen, F. Wang, S. G. Louie, M. F. Crommie, *Nat. Mater.* **2014**, *13*, 1091.
[62] B. Zhu, X. Chen, X. Cui, *Sci. Rep.* **2015**, *5*, 9218.
[63] H. M. Hill, A. F. Rigosi, C. Roquelet, A. Chernikov, T. C. Berkelbach, D. R. Reichman, M. S. Hybertsen, L. E. Brus, T. F. Heinz, *Nano Lett.* **2015**, *15*, 2992.
[64] A. M. Jones, H. Yu, N. J. Ghimire, S. Wu, G. Aivazian, J. S. Ross, B. Zhao, J. Yan, D. G. Mandrus, D. Xiao, W. Yao, X. Xu, *Nat. Nanotechnol.* **2013**, *8*, 634.
[65] H. J. Liu, L. Jiao, L. Xie, F. Yang, J. L. Chen, W. K. Ho, C. L. Gao, J. F. Jia, X. D. Cui, M. H. Xie, *2D Mater.* **2015**, *2*, 034004.
[66] J. Pei, J. Yang, R. Xu, Y.-H. Zeng, Y. W. Myint, S. Zhang, J.-C. Zheng, Q. Qin, X. Wang, W. Jiang, Y. Lu, *Small* **2015**, *11*, 6384.
[67] A. Singh, G. Moody, S. Wu, Y. Wu, N. J. Ghimire, J. Yan, D. G. Mandrus, X. Xu, X. Li, *Phys. Rev. Lett.* **2014**, *112*, 216804.
[68] C. Riva, F. M. Peeters, K. Varga, *Phys. Rev. B* **2000**, *61*, 13873.

[69] R. Matsunaga, K. Matsuda, Y. Kanemitsu, *Phys. Rev. Lett.* **2011**, *106*, 037404.
[70] T. Kato, T. Kaneko, *ACS Nano* **2016**, *10*, 9687.
[71] J. He, D. He, Y. Wang, Q. Cui, M. Z. Bellus, H.-Y. Chiu, H. Zhao, *ACS Nano* **2015**, *9*, 6436.
[72] J. He, D. He, Y. Wang, Q. Cui, F. Ceballos, H. Zhao, *Nanoscale* **2015**, *7*, 9526.
[73] N. Kumar, Q. Cui, F. Ceballos, D. He, Y. Wang, H. Zhao, *Nanoscale* **2014**, *6*, 4915.
[74] B. Liao, H. Zhao, E. Najafi, X. Yan, H. Tian, J. Tice, A. J. Minnich, H. Wang, A. H. Zewail, *Nano Lett.* **2017**, *17*, 3675.
[75] D. Sanvitto, F. Pulizzi, A. J. Shields, P. C. M. Christianen, S. N. Holmes, M. Y. Simmons, D. A. Ritchie, J. C. Maan, M. Pepper, *Science* **2001**, *294*, 837.
[76] G. M. Akselrod, P. B. Deotare, N. J. Thompson, J. Lee, W. A. Tisdale, M. A. Baldo, V. M. Menon, V. Bulović, *Nat. Commun.* **2014**, *5*, 3646.
[77] H. Liu, A. T. Neal, Z. Zhu, Z. Luo, X. Xu, D. Tománek, P. D. Ye, *ACS Nano* **2014**, *8*, 4033.
[78] Q. Cui, F. Ceballos, N. Kumar, H. Zhao, *ACS Nano* **2014**, *8*, 2970.
[79] H. S. Lee, S.-W. Min, Y.-G. Chang, M. K. Park, T. Nam, H. Kim, J. H. Kim, S. Ryu, S. Im, *Nano Lett.* **2012**, *12*, 3695.
[80] S. Tongay, J. Zhou, C. Ataca, K. Lo, T. S. Matthews, J. Li, J. C. Grossman, J. Wu, *Nano Lett.* **2012**, *12*, 5576.
[81] H. J. Conley, B. Wang, J. I. Ziegler, R. F. Haglund, S. T. Pantelides, K. I. Bolotin, *Nano Lett.* **2013**, *13*, 3626.
[82] S. B. Desai, G. Seol, J. S. Kang, H. Fang, C. Battaglia, R. Kapadia, J. W. Ager, J. Guo, A. Javey, *Nano Lett.* **2014**, *14*, 4592.
[83] R. Fei, L. Yang, *Nano Lett.* **2014**, *14*, 2884.
[84] J. Quereda, P. San-Jose, V. Parente, L. Vaquero-Garzon, A. J. Molina-Mendoza, N. Agraït, G. Rubio-Bollinger, F. Guinea, R. Roldán, A. Castellanos-Gomez, *Nano Lett.* **2016**, *16*, 2931.
[85] C. Wang, Q. Xia, Y. Nie, G. Guo, *J. Appl. Phys.* **2015**, *117*, 124302.
[86] M. Sharma, A. Kumar, P. K. Ahluwalia, R. Pandey, *J. Appl. Phys.* **2014**, *116*, 063711.
[87] M. Z. Bellus, F. Ceballos, H.-Y. Chiu, H. Zhao, *ACS Nano* **2015**, *9*, 6459.
[88] L. Britnell, R. M. Ribeiro, A. Eckmann, R. Jalil, B. D. Belle, A. Mishchenko, Y.-J. Kim, R. V. Gorbachev, T. Georgiou, S. V. Morozov, A. N. Grigorenko, A. K. Geim, C. Casiraghi, A. H. C. Neto, K. S. Novoselov, *Science* **2013**, *340*, 1311.
[89] K. Chen, X. Wan, W. Xie, J. Wen, Z. Kang, X. Zeng, H. Chen, J. Xu, *Adv. Mater.* **2015**, *27*, 6431.
[90] Y. Deng, Z. Luo, N. J. Conrad, H. Liu, Y. Gong, S. Najmaei, P. M. Ajayan, J. Lou, X. Xu, P. D. Ye, *ACS Nano* **2014**, *8*, 8292.
[91] Y. Gong, J. Lin, X. Wang, G. Shi, S. Lei, Z. Lin, X. Zou, G. Ye, R. Vajtai, B. I. Yakobson, H. Terrones, M. Terrones, B. K. Tay, J. Lou, S. T. Pantelides, Z. Liu, W. Zhou, P. M. Ajayan, *Nat. Mater.* **2014**, *13*, 1135.
[92] X. Hong, J. Kim, S.-F. Shi, Y. Zhang, C. Jin, Y. Sun, S. Tongay, J. Wu, Y. Zhang, F. Wang, *Nat. Nanotechnol.* **2014**, *9*, 682.
[93] M. Massicotte, P. Schmidt, F. Vialla, K. G. Schädler, A. Reserbat-Plantey, K. Watanabe, T. Taniguchi, K. J. Tielrooij, F. H. L. Koppens, *Nat. Nanotechnol.* **2015**, *11*, 42.
[94] K. S. Novoselov, A. H. C. Neto, *Phys. Scr.* **2012**, *2012*, 014006.
[95] P. Rivera, J. R. Schaibley, A. M. Jones, J. S. Ross, S. Wu, G. Aivazian, P. Klement, K. Seyler, G. Clark, N. J. Ghimire, J. Yan, D. G. Mandrus, W. Yao, X. Xu, *Nat. Commun.* **2015**, *6*, 6242.
[96] F. Withers, O. Del Pozo-Zamudio, A. Mishchenko, A. P. Rooney, A. Gholinia, K. Watanabe, T. Taniguchi, S. J. Haigh, A. K. Geim, A. I. Tartakovskii, K. S. Novoselov, *Nat. Mater.* **2015**, *14*, 301.
[97] H.-P. Komsa, J. Kotakoski, S. Kurasch, O. Lehtinen, U. Kaiser, A. V. Krasheninnikov, *Phys. Rev. Lett.* **2012**, *109*, 035503.
[98] H. Nan, Z. Wang, W. Wang, Z. Liang, Y. Lu, Q. Chen, D. He, P. Tan, F. Miao, X. Wang, J. Wang, Z. Ni, *ACS Nano* **2014**, *8*, 5738.
[99] J. Pei, X. Gai, J. Yang, X. Wang, Z. Yu, D.-Y. Choi, B. Luther-Davies, Y. Lu, *Nat. Commun.* **2016**, *7*, 10450.
[100] H. Qiu, T. Xu, Z. Wang, W. Ren, H. Nan, Z. Ni, Q. Chen, S. Yuan, F. Miao, F. Song, G. Long, Y. Shi, L. Sun, J. Wang, X. Wang, *Nat. Commun.* **2013**, *4*, 2642.
[101] J. Xie, H. Zhang, S. Li, R. Wang, X. Sun, M. Zhou, J. Zhou, X. W. Lou, Y. Xie, *Adv. Mater.* **2013**, *25*, 5807.
[102] J. Xie, J. Zhang, S. Li, F. Grote, X. Zhang, H. Zhang, R. Wang, Y. Lei, B. Pan, Y. Xie, *J. Am. Chem. Soc.* **2013**, *135*, 17881.
[103] W. Zhou, X. Zou, S. Najmaei, Z. Liu, Y. Shi, J. Kong, J. Lou, P. M. Ajayan, B. I. Yakobson, J.-C. Idrobo, *Nano Lett.* **2013**, *13*, 2615.
[104] A. Ziletti, A. Carvalho, D. K. Campbell, D. F. Coker, A. H. Castro Neto, *Phys. Rev. Lett.* **2015**, *114*, 046801.
[105] A. Ziletti, A. Carvalho, P. E. Trevisanutto, D. K. Campbell, D. F. Coker, A. H. Castro Neto, *Phys. Rev. B* **2015**, *91*, 085407.
[106] X. L. Yang, S. H. Guo, F. T. Chan, K. W. Wong, W. Y. Ching, *Phys. Rev. A* **1991**, *43*, 1186.
[107] N. Scheuschner, O. Ochedowski, A.-M. Kaulitz, R. Gillen, M. Schleberger, J. Maultzsch, *Phys. Rev. B* **2014**, *89*, 125406.
[108] H. Shi, R. Yan, S. Bertolazzi, J. Brivio, B. Gao, A. Kis, D. Jena, H. G. Xing, L. Huang, *ACS Nano* **2013**, *7*, 1072.
[109] M. Amani, D.-H. Lien, D. Kiriya, J. Xiao, A. Azcatl, J. Noh, S. R. Madhvapathy, R. Addou, S. KC, M. Dubey, K. Cho, R. M. Wallace, S.-C. Lee, J.-H. He, J. W. Ager, X. Zhang, E. Yablonovitch, A. Javey, *Science* **2015**, *350*, 1065.
[110] Z. Li, S.-W. Chang, C.-C. Chen, S. B. Cronin, *Nano Res.* **2014**, *7*, 973.
[111] S. Lu, Y. Ge, Z. Sun, Z. Huang, R. Cao, C. Zhao, S. Wen, D. Fan, J. Li, H. Zhang, *Photonics Res.* **2016**, *4*, 286.
[112] A. A. Mitioglu, P. Plochocka, Á. Granados del Aguila, P. C. M. Christianen, G. Deligeorgis, S. Anghel, L. Kulyuk, D. K. Maude, *Nano Lett.* **2015**, *15*, 4387.
[113] R. Xu, J. Yang, Y. W. Myint, J. Pei, H. Yan, F. Wang, Y. Lu, *Adv. Mater.* **2016**, *28*, 3493.
[114] R. Xu, J. Yang, Y. Zhu, H. Yan, J. Pei, Y. W. Myint, S. Zhang, Y. Lu, *Nanoscale* **2016**, *8*, 129.
[115] O. A. Dyatlova, J. Gomis-Bresco, E. Malic, H. Telg, J. Maultzsch, G. Zhong, J. Geng, U. Woggon, *Phys. Rev. B* **2012**, *85*, 245449.
[116] V. Perebeinos, J. Tersoff, P. Avouris, *Phys. Rev. Lett.* **2004**, *92*, 257402.
[117] Y. Yu, S. Hu, L. Su, L. Huang, Y. Liu, Z. Jin, A. A. Purezky, D. B. Geohegan, K. W. Kim, Y. Zhang, L. Cao, *Nano Lett.* **2015**, *15*, 486.
[118] B. W. H. Baugher, H. O. H. Churchill, Y. Yang, P. Jarillo-Herrero, *Nat. Nanotechnol.* **2014**, *9*, 262.
[119] Z. Chu, J. Liu, Z. Guo, H. Zhang, *Opt. Mater. Express* **2016**, *6*, 2374.
[120] M. Koperski, K. Nogajewski, A. Arora, V. Cherkez, P. Mallet, J. Y. Veuillen, J. Marcus, P. Kossacki, M. Potemski, *Nat. Nanotechnol.* **2015**, *10*, 503.
[121] H. Mu, S. Lin, Z. Wang, S. Xiao, P. Li, Y. Chen, H. Zhang, H. Bao, S. P. Lau, C. Pan, D. Fan, Q. Bao, *Adv. Opt. Mater.* **2015**, *3*, 1447.
[122] Y. Ye, Z. J. Wong, X. Lu, X. Ni, H. Zhu, X. Chen, Y. Wang, X. Zhang, *Nat. Photonics* **2015**, *9*, 733.
[123] S. Wu, S. Buckley, J. R. Schaibley, L. Feng, J. Yan, D. G. Mandrus, F. Hatami, W. Yao, J. Vučković, A. Majumdar, X. Xu, *Nature* **2015**, *520*, 69.
[124] A. Pospischil, M. M. Furchi, T. Mueller, *Nat. Nanotechnol.* **2014**, *9*, 257.
[125] J. S. Ross, P. Klement, A. M. Jones, N. J. Ghimire, J. Yan, D. G. Mandrus, T. Taniguchi, K. Watanabe, K. Kitamura, W. Yao, D. H. Cobden, X. Xu, *Nat. Nanotechnol.* **2014**, *9*, 268.
[126] S. C. Dhanabalan, J. S. Ponraj, H. Zhang, Q. Bao, *Nanoscale* **2016**, *8*, 6410.

[127] O. Lopez-Sanchez, D. Lembke, M. Kayci, A. Radenovic, A. Kis, *Nat. Nanotechnol.* **2013**, *8*, 497.
[128] X. Ren, Z. Li, Z. Huang, D. Sang, H. Qiao, X. Qi, J. Li, J. Zhong, H. Zhang, *Adv. Funct. Mater.* **2017**, *27*, 1606834.
[129] S. B. Lu, L. L. Miao, Z. N. Guo, X. Qi, C. J. Zhao, H. Zhang, S. C. Wen, D. Y. Tang, D. Y. Fan, *Opt. Express* **2015**, *23*, 11183.
[130] H. Zhang, D. Y. Tang, L. M. Zhao, Q. L. Bao, K. P. Loh, *Opt. Express* **2009**, *17*, 17630.
[131] L. Zhang, R. Gogna, W. Burg, E. Tutuc, H. Deng, *Nat. Commun.* **2018**, *9*, 713.
[132] C. H. Lee, G. H. Lee, A. M. van der Zande, W. Chen, Y. Li, M. Han, X. Cui, G. Arefe, C. Nuckolls, T. F. Heinz, J. Guo, J. Hone, P. Kim, *Nat. Nanotechnol.* **2014**, *9*, 676.
[133] S. Wang, J. Wang, W. Zhao, F. Giustiniano, L. Chu, I. Verzhbitskiy, J. Zhou Yong, G. Eda, *Nano Lett.* **2017**, *17*, 5156.
[134] Y. Yu, F. Miao, J. He, Z. Ni, *Chin. Phys. B* **2017**, *26*, 036801.
[135] M. L. Tsai, S. H. Su, J. K. Chang, D. S. Tsai, C. H. Chen, C. I. Wu, L. J. Li, L. J. Chen, J. H. He, *ACS Nano* **2014**, *8*, 8317.
[136] W. J. Yu, Y. Liu, H. Zhou, A. Yin, Z. Li, Y. Huang, X. Duan, *Nat. Nanotechnol.* **2013**, *8*, 952.
[137] F. Gong, W. Luo, J. Wang, P. Wang, H. Fang, D. Zheng, N. Guo, J. Wang, M. Luo, J. C. Ho, X. Chen, W. Lu, L. Liao, W. Hu, *Adv. Funct. Mater.* **2016**, *26*, 6084.
[138] N. Huo, G. Konstantatos, *Nat. Commun.* **2017**, *8*, 572.
[139] M. Huang, M. Wang, C. Chen, Z. Ma, X. Li, J. Han, Y. Wu, *Adv. Mater.* **2016**, *28*, 3481.
[140] X. Chen, X. Lu, B. Deng, O. Sinai, Y. Shao, C. Li, S. Yuan, V. Tran, K. Watanabe, T. Taniguchi, D. Naveh, L. Yang, F. Xia, *Nat. Commun.* **2017**, *8*, 1672.
[141] L. Wang, L. Huang, W. C. Tan, X. Feng, L. Chen, X. Huang, K.-W. Ang, *Small Methods* **2018**, *2*, 1700294.
[142] C. Xie, C. Mak, X. Tao, F. Yan, *Adv. Funct. Mater.* **2017**, *27*, 1603886.
[143] H. Zhang, S. B. Lu, J. Zheng, J. Du, S. C. Wen, D. Y. Tang, K. P. Loh, *Opt. Express* **2014**, *22*, 7249.
[144] Q. Bao, H. Zhang, Y. Wang, Z. Ni, Y. Yan, Z. X. Shen, K. P. Loh, D. Y. Tang, *Adv. Funct. Mater.* **2009**, *19*, 3077.
[145] Y. Chen, G. Jiang, S. Chen, Z. Guo, X. Yu, C. Zhao, H. Zhang, Q. Bao, S. Wen, D. Tang, D. Fan, *Opt. Express* **2015**, *23*, 12823.
[146] Z. Qin, G. Xie, C. Zhao, S. Wen, P. Yuan, L. Qian, *Opt. Lett.* **2016**, *41*, 56.
[147] H. Yu, D. Talukdar, W. Xu, J. B. Khurgin, Q. Xiong, *Nano Lett.* **2015**, *15*, 5653.
[148] C. Lin, R. Grassi, T. Low, A. S. Helmy, *Nano Lett.* **2016**, *16*, 1683.
[149] W. S. Whitney, M. C. Sherrott, D. Jariwala, W. H. Lin, H. A. Bechtel, G. R. Rossman, H. A. Atwater, *Nano Lett.* **2017**, *17*, 78.
[150] M. Tahir, P. Vasilopoulos, *Phys. Rev. B* **2016**, *94*.
[151] Y. Li, Z. Li, C. Chi, H. Shan, L. Zheng, Z. Fang, *Adv. Sci.* **2017**, *4*, 1600430.
[152] Z. Sun, A. Martinez, F. Wang, *Nat. Photonics* **2016**, *10*, 227.